APPLICATION OF DETERMINISTIC 3D S_N TRANSPORT DRIVEN

DOSE KERNEL METHODS FOR

OUT-OF-FIELD DOSE ASSESSMENTS IN CLINICAL

MEGAVOLTAGE RADIATION THERAPY

A Dissertation
Presented to
The Academic Faculty

by

Mi Huang

In Partial Fulfillment
of the Requirements for the Degree
Doctor of Philosophy in the
School of Nuclear and Radiological Engineering

Georgia Institute of Technology
December 2015

APPLICATION OF DETERMINISTIC 3D S_N TRANSPORT DRIVEN

DOSE KERNEL METHODS FOR

OUT-OF-FIELD DOSE ASSESSMENTS IN CLINICAL

MEGAVOLTAGE RADIATION THERAPY

Approved by:

Dr. C-K Chris Wang, Advisor
School of Mechanical Engineering
Georgia Institute of Technology

Dr. Eric Elder
School of Mechanical Engineering
Georgia Institute of Technology
Emory University

Dr. Anees Dhabaan
School of Mechanical Engineering
Georgia Institute of Technology
Emory University

Dr. Timothy Fox
School of Mechanical Engineering
Georgia Institute of Technology
Emory University
Varian Medical Systems

Dr. Jonathan G. Li
Radiation Oncology
University of Florida

Dr. Glenn Sjoden
Air Force Tech. Applications Center

Date Approved: August 12, 2015

I dedicate this thesis work to my beloved parents and my close family, for supporting me with everlasting love and affection. I am who I am today with your education.
To my mentors, all my family and friends, I couldn't have done this without you. Thank you for the encouragement and support along every footstep of my life.

ACKNOWLEDGEMENTS

TABLE OF CONTENTS

LIST OF TABLES

LIST OF FIGURES

LIST OF SYMBOLS AND ABBREVIATIONS

H	Forward Transport Operator
ψ_g	Angular Flux in group G
S_g	Source rate in group G
ψ^*	Adjoint Function
AAA	Anisotropic Analytical Algorithm
ALRADS	Advanced Laboratory for Radiation Dosimetry Studies (U. Florida)
Al_2O_3	Aluminum Oxide
API	Application Programming Interface
BEAMnrc	Radiation Beam Modeling Tool by National Research Council (Ca)
BRM	Beam Reconstruction Model
CAD	Computer-aided Design
CEPXS	A Sandia National Laboratory Multi-group Photon/Electron XS Code
CC	Collapsed Cone Superposition Convolution
CT	Computed Tomography
DDV	Dose-Driving Voxel
DO	Discrete Ordinates Transport
EDK-S_N	Electron Dose Kernel driven by S_N transport
EGSnrc	Electron Gamma Shower National Research Council (Ca)
ENDF	Evaluated Nuclear Data File
FWHM	Full Width at Half-Maximum
GEANT4	**GE**ometry **an**d **T**racking Monte Carlo Tool by CERN
GBD	Golden Beam Data

HDF5	Hierarchical Data Format 5
IAEA	International Atomic Energy Agency
IC	Icosahedral Quadratures
ICRU	International Commission on Radiation Units & Measurements
IMRT	Intensity-Modulated Radiation Therapy
LBE	Linear Boltzmann Equation
LiF	Lithium Fluoride
MC	Monte Carlo
MDCT	Multiple Detector Computed Tomography
MLC	Multileaf Collimator
MOC	Method of Characteristics
NCRP	National Council on Radiation Protection & Measurements
OAR	Organ at Risk
OSLD	Optically Stimulated Thermoluminescent Dosimeter
PACE	Georgia Tech's Partnership for Advanced Computing Environment
PBC	Pencil Beam Convolution
PENTRAN	Parallel Environment Transport
PENTRAN-CRT	Parallel Environment Transport w/ Characteristic Ray Tracing
PDD	Percent Depth Dose
PDF	Probability Distribution Function
PHSPMC	Phase Space to Monte Carlo Software Framework
phsp	IAEA Phase Space label
Pn-Tn	Legendre-Chebyshev Quadrature
PyNE	Python for Nuclear Engineering
TAR	Tissue Air Ratio

TB	Terabyte
TLD	Thermoluminescent Dosimeter
TPS	Treatment Planning System
RSEL	Radiological Science and Engineering Laboratory
S_N	Discrete Ordinates Transport
SPD	Source-to-Patient Distance
SSD	Surface-to-Source Distance
VCLA	Varian Clinac Linear Accelerator

SUMMARY

With the recent interest in single fraction Stereotactic Body Radiation Therapy and the emerging prominence of the Rapid Arc radiotherapy technique capable of delivering a fast and accurate treatment, the in-field primary dose and out-of-field dose assessments are becoming increasingly important. Currently, full physics Monte Carlo calculations for dose calculations have been regarded as a 'gold standard' for dose assessments of the target and OAR (organ at risk). However, these Monte Carlo calculations require very long computation times. The current treatment planning methods provide shorter calculation times, but issues such as heterogeneities and model-based parameter calculations cause challenges and affect dose calculation accuracy. This thesis describes a new and fast dose estimation method leveraging parallel computing called EDK-S_N, "Electron Dose Kernel-Discrete Ordinates". This new method uses hybrid electron dose kernels driven by linear Boltzmann (discrete ordinates) photon transport method to carry out dose calculations. The method has proven effective for fast and accurate computations of out-of-field whole body dose calculations benchmarked to Monte Carlo with isotropic monoenergetic photon sources.

This thesis accomplishes adaptation of clinical Varian phase space data for use with general Monte Carlo codes including MCNP, and mapping accurate phase space data into the application of optimized EDK-S_N dose calculation method with a 15-year-old patient phantom. The EDK-S_N method with improved source term modeling is demonstrated to fall within accuracy of the measured golden beam data for a clinical water phantom.

CHAPTER 1

INTRODUCTION

With the recent interest in Intensity-Modulated Radiation Therapy (IMRT) and Stereotactic Body Radiation Therapy (SBRT), capable of delivering fast and accurate radiotherapy treatments, quantification of in-field (primary) dose and out-of-field (leakage and scattered) dose is increasingly important to the radiation therapy physics community. Accurate dose in both measurement and computation contributes significantly to treatment plan quality and also to maximizing dose to the patient tumor. In particular, the estimation of out-of-field dose is increasingly important with the associated increase of monitor units, again, with the popularity of IMRT, and quantification of late effects quantifiable to doses as low as 5 cGy in a pregnant patient fetus (Stovall, Blackwell et al. 1995, Kry, Titt et al. 2006).

Currently, full physics Monte Carlo calculations for dose estimation have been regarded as a 'gold standard' for dose assessments of the target and OAR (organ at risk) (Varian 2011). However, full physics Monte Carlo calculations typically require very long computation times. It is true that current treatment planning methods provide much shorter calculation times such as Anisotropic Analytical Algorithm (AAA), Pencil Beam Convolution (PBC), and Collapsed Cone Superposition Convolution (CC); however, issues such as heterogeneities and model-based parameter calculations can lead to significant challenges and affect dose calculation accuracy.

In this dissertation, a new and fast dose estimation method leveraging parallel computing called EDK-S_N, "Electron Dose Kernel-Discrete Ordinates" is applied and improved for clinical applications. This new method uses hybrid electron dose kernels driven by linear Boltzmann (discrete ordinates) photon transport method to carry out dose calculations. The method has proven effective for fast and accurate computations of whole body dose calculations

1

benchmarked to Monte Carlo with simple isotropic monoenergetic photon sources. This thesis focuses on the development of a fully optimized EDK-S_N dose calculation method applied with real clinical sources and standards with phantom validation. The research also analyzed the impact of different spatial and angular S_N grids to determine dose, combined with an optimally discretized energy spectrum using the real Varian Clinac head model from the Varian Clinical Linear Accelerator (VCLA) Laboratory housed in the Radiological Science and Engineering Laboratory (RSEL) at Georgia Tech. Moreover, the results obtained from this new method are compared with the results obtained from the full physics photon-electron Monte Carlo code, MCNP. The work will culminate in a fully validated EDK-S_N methodology applied to real clinical protocols and validated with Monte Carlo.

1.1 Thesis Significance

Full physics Monte Carlo calculations for in-field and out-of-field dose calculations have been regarded as a 'gold standard' for dose assessments of the cellular target region and OAR (organ at risk). However, these Monte Carlo calculations require very long computation times. Alternatively, "model" based algorithms are available; the current Anisotropic Analytical Algorithm, also initialized as AAA, (Varian 2011) and Pencil Beam Convolution Algorithm (PBC) can each provide shorter calculation times with comparable results, but heterogeneities may challenge dose calculation accuracy, sacrificing up to 20% error in small in-field regions (Chetty, Curran et al. 2007). Any model-based source also inherently sacrifices accuracy. The out-of-field dose calculation can lead up to 15% (Chetty, Curran et al. 2007) error in the model-based algorithm computed doses compared to actual dose measurements. Recently, the Acuros XB system has been adapted and integrated into the Varian Medical Systems Treatment Planning System (TPS) with the intention to resolve heterogeneities in different mediums, providing results comparable to full Monte Carlo. However, the Acuros XB algorithm has adapted the AAA linear accelerator parameters, using the mathematical Gaussian kernel approximation of the photon source distribution (Failla, Wareing et al. 2011), and does not fully

2

model the Linac head source particle distribution for individual particles, including photons, electrons, and protons, for energy, space and angle distributions. Also, this approach sacrifices, to a certain extent, the large field and out-of-field dose calculation accuracy due to deterministic transport calculation round up when dealing with photon-electron coupled transport calculations. Hence, while the approach used in Acuros XB improves speed, it still sacrifices accuracy compared to the traditional, full physics Monte Carlo calculations.

This thesis applies a new, fast convergence dose estimation approach leveraging parallel computing called "EDK-S_N", more specifically an "Electron Dose Kernel" discrete ordinates (DO) calculation. This novel approach uses hybrid electron dose kernels solved by linear Boltzmann (discrete ordinates) photon transport method for heterogeneous, voxelized phantoms in a parallel computing environment to carry out radiotherapy dose calculations. Prior to this work, the EDK-S_N method was demonstrated to be effective for fast and accurate computations of in-field and out-of-field whole body dose calculations for simple test sources (Al Basheer 2008). Evolving on that effort, this thesis further refines and adapts the EDK-Sn methodology with application to clinically relevant cases and phantoms. The results obtained with this new method have demonstrated independent agreement with the results obtained from the Monte Carlo photon-electron transport calculations for the selected organ doses from a 15-year-old computational male patient phantom. The EDK-S_N method yields a speedup of ~8 (e.g. 1 hour versus 8+ hours) over traditional parallel full physics Monte Carlo, with less than 10% difference of the predicted dose noted in homogeneous materials, and up to 20% in heterogeneous media (smaller given stochastic uncertainties). Furthermore, the EDK-S_N method splits the beam into discrete angles, energy, and space, therefore performs fast convergence on a discretized Cartesian grid based on distributed high performance computing photon transport, reducing global error when compared with a Monte Carlo computation using the same parallel computational resources.

1.2 Chapter Organization

Chapter 2 provides literature review and background for model-based calculation methods in treatment system planning practice. Chapter 3 describes the deterministic transport methods used for EDK-S_N. Chapter 4 describes the improvements over the original EDK-S_N method and the validation of EDK to golden beam data. Chapter 5 discusses how the PHSPMC software enables the use of Varian-based Phase Space data in the Monte Carlo code applications. Chapter 6 describes the Varian-based Phase Space Application to a 15-year old male phantom, using both the EDK-S_N method and the Monte Carlo code MCNP, and showing an advantage of the EDK-S_N method over the MCNP. Finally, the conclusions of the thesis are provided in Chapter 7.

CHAPTER 2

LITERATURE REVIEW AND BACKGROUND

This chapter provides a brief review of the current methods used in the commercially available TPS for radiotherapy. These methods are used to compare and contrast the results obtained using the EDK-S_N method.

2.1 Model-based Calculation Methods Used in Varian Treatment Planning System

The following model-based photon treatment 3D absorbed dose calculations are currently/widely adapted in Varian Treatment Planning Systems (8.0 and newer versions).

2.1.1 Model based Anisotropic Analytical Algorithm (AAA)

The Anisotropic Analytical Algorithm (AAA) (Ulmer and Harder 1995, Sievinen, Ulmer et al. 2005, Varian 2011) is a convolution superposition algorithm using three-dimensional beamlets. The underlying mechanism for photon modeling is that the primary photon beams are determined using the Monte Carlo method. The AAA is a 3D pencil-beam kernel-based superposition algorithm (Ulmer, 2005), and includes separately modeled Linac head contributions from three separate sources: primary photons, extra-focal photons and contaminating electrons. Each of the three sources has an associated fluence, an energy deposition density function, and a scatter kernel. Six exponential and Gaussian curves are used to model the characteristics of dose distribution (Ulmer, 2000).

Two important calculation parts are defined in the convolution algorithms: TERMA (total energy released per unit mass), which describes the energy deposited to the medium by the interactions of primary photons, and a scattering dose kernel, which describes the energy

deposited about a primary photon interaction site. The dose at any point can be calculated from the convolution of the TERMA with the kernel:

$$D(\vec{r}) = \int \frac{\mu}{\rho} \psi(\vec{r}) K(\vec{r} - \vec{r}') d\mathbf{r} = T_p(\vec{r}) K(\vec{r} - \vec{r}') d\mathbf{r} \qquad (1)$$

To be more specific,

$$D(\vec{r}) = \int \frac{\mu}{\rho} \psi(\vec{r}) K(\vec{r} - \vec{r}') d\mathbf{r} = T_p(\rho_{\vec{r}}(\vec{r})) K(\rho_{\vec{r}-\vec{r}'}(\vec{r} - \vec{r}')) d\mathbf{r} \qquad (2)$$

$T_p(\vec{r})$ is the TERMA, which is the photon fluence $\psi(\vec{r})$, scaled by the mass attenuation coefficient $\frac{\mu}{\rho}$. The term $K(\vec{r} - \vec{r}') d\mathbf{r}$ is the scattering kernel at each point, and $(\rho_{\vec{r}-\vec{r}'}(\vec{r} - \vec{r}'))$ is the radiologic distance from the dose deposition site to the primary photon interaction site.

In Varian Eclipse TPS, the dose calculation algorithm calculates the dose deposition using the fundamental physical parameters determined from the configuration algorithm. The clinical beam is also divided into beamlets, each having a beamlet intensity. For each beamlet, energy deposition is calculated using an "energy deposition density" function convoluted by a pre-calculated photon scattering kernel, which is parameterized. The volumetric dose distribution is calculated for the patient body volume via a matrix of three dimensional calculation voxels utilizing a specific calculation grid. The voxels are aligned such that they are divergent along the beam fan-lines. Each voxel has a density ρ, determined from CT images. The density is the same in each organ for heterogeneous CTs. The convolutions are then performed on all beamlets, which compose the clinical beam. The final absorbed dose is the superposition of all individual beamlet convolutions, and is computed from primary photons and the extra-focal photons, as well as the contamination from electrons (Varian 2011).

Good agreement is obtained between the true Monte Carlo calculation results. However, the AAA also has a tendency to overestimate the dose to a denser medium following passage

through less dense tissue, such as the lung. Effects vary with field size. The smaller the tumor, the larger the difference between the AAA and the true Monte Carlo calculation results. However, as discussed below, in terms of handling inhomogeneous cases such as lung tissue, the AAA is still favored over the Pencil Beam Convolution Algorithm (PBC). In addition, the Pinnacle Collapsed Cone Algorithm is very similar to the AAA in terms of performance, however, improving on heterogeneous correction (Ulmer and Harder 1995, Miften, Wiesmeyer et al. 2001, Sievinen, Ulmer et al. 2005, Fogliata, Vanetti et al. 2007).

2.1.2 Model-based Pencil Beam Convolution Algorithm (PBC)

Prior to the AAA algorithm, the PBC algorithm (Ahnesjö, Saxner et al. 1992) was developed. Similar to the AAA, the PBC algorithm is based on pencil beam kernel convolution. However, in terms of handling modeling of lateral electron transport directly in the AAA, the PBC used simplified heterogeneity correction method based on the relative electron densities based on CT scans. Three density correction methods have been used: Batho Power Law (PBC-BPL), Modified Batho (PBC-MB), and Equivalent Tissue Air Ratio (PBC-ETAR). First, a relative dose distribution was calculated within a homogenous water equivalent phantom, then an inhomogeneity correction factor (ICF) was applied. This factor corrects for the variation in tissue density. ICF is defined as the dose in a heterogeneous medium divided by the dose at the same point for homogenous phantoms. Specific correction methods were discussed in the references provided (Batho 1964, El-Khatib and Battista 1984, Wong and Purdy 1990, Thomas 1991, Ahnesjö and Aspradakis 1999, Papanikolaou, Battista et al. 2004). The PBC algorithm does not model the lateral spread of the full physics of the scattering kernels, and uses correction-based patient heterogeneities calculation in terms of modeling lateral electron spread in 3D scattering kernels, which is typically less accurate compared to the AAA method (Fogliata, Vanetti et al. 2007).

2.1.3 Model-based Electron Dose Calculation Method – Generalized Gaussian Pencil Beam Algorithm

The Generalized Gaussian Pencil Beam (Lax 1987, Hyödynmaa 1994) algorithm was derived from the Fermi-Eyges electron multiple scattering theories. The radial absorbed dose distribution is calculated as a sum of three Gaussian functions(Varian 2011). This takes into account large-angle scattering and range straggling. For a three dimensional implementation, the integration of absorbed dose is replaced with summation of a set of square pencil beams uniformly distributed throughout the entire field. Pencil beams outside the field are also included in the calculation to take into account for in-air scattering. The intersection with patient and the fan-line are calculated first. If the pencil beam is blocked and the weight of the beam is smaller than the relative value of the electron depth dose of the blocked beam at the surface, the electron depth dose of a blocked beam is used. The dose contribution from each pencil beam is summed to the point of calculation matrix. The calculation matrix represents a plane in the object. The final step is to add the bremsstrahlung to the dose distribution as a photon field. The bremsstrahlung contribution does not take into account the inhomogeneity effect.

2.1.4 Monte Carlo Method

General-purpose Monte Carlo codes used in Medical Physics include MCNP6, GEANT4, EGSnrc, and PENELOPE. The Monte Carlo full physics dose calculation is usually very time consuming compared to the aforementioned methods. Currently, the accuracy of the Monte Carlo calculation is the highest, especially in heterogeneous regions. The difference between Monte Carlo calculations and other commercial codes could be up to 15-20% (Krieger and Sauer 2005, Chetty, Curran et al. 2007).

2.1.5 Acuros: Deterministic Transport in Treatment Planning

The Acuros dose calculation method (Bush, Gagne et al. 2011, Failla, Wareing et al. 2011) for the Eclipse treatment planning system is based on solving the governing equation:

Linear Boltzmann equation (LBE) for photon and electron transport. The background discussion for deterministic transport is provided in Chapter 3. Acuros XB is adapted from the discrete ordinates (S_N) transport code Attila.

Acuros adapted the AAA model based Linac head model; it performs a fast calculation compared to full Monte Carlo simulation, however at the cost of losing full particle physics information from the Linac head. Acuros XB directly calculates the absorbed dose in the heterogeneous medium, therefore showing better agreement with the Monte Carlo method than the model based calculation methods. However, The electron-photon coupled transport does not include bremsstrahlung generated by the electrons, and therefore will compromise some accuracy in the calculation (Bush, Gagne et al. 2011, Failla, Wareing et al. 2011). Also, fully coupled deterministic photon-electron computations have shown to be challenging to fully achieve local convergence based on various S_N orders and electron cross sections (Dionne 2007). While the heterogeneous correction in Acuros does yield better results than the aforementioned model-based algorithms due to the use of S_N transport, the out-of-field accuracy has not been fully evaluated in this system at present.

CHAPTER 3

DETERMINISTIC TRANSPORT FUNDAMENTALS

This chapter discusses the necessary fundamentals of deterministic transport method and it serves as a prerequisite for the discussion of the EDK-S_N method in the next chapter. The latter portion of this chapter also introduces the Georgia Tech Varian Clinac, where Appendix A provides a specific application of adjoint detector response. The intent of Appendix A is to demonstrate the tremendous effort required in obtaining suitable multi-group cross sections for medical physics and shielding-related applications.

3.1 Deterministic Transport Method

The Boltzmann transport equation was originally derived to solve particle balance between molecular dynamics of gases. It can also be used to derive a balance of particles for electron transport. As it pertains to this thesis, electron transport, simulated by using a Monte Carlo driven kernel that indirectly solves the electron transport equation, is driven by photon fluxes solved using the 3D discrete ordinates code PENTRAN.

3.1.1   Linear Boltzmann Transport Equation

There are many ways to go about presenting the linear Boltzmann transport equation; in this thesis, the starting basis is time-independent form of the equation, which describes the balance of photons (but would also apply to neutrons) at position $\vec{r}$ and energy E oriented along direction $\hat{\Omega}$ (Bell and Glasstone 1970):

$$\sigma_t\left(\bar{r},E\right)\psi\left(\bar{r},E,\hat{\Omega}\right)+\hat{\Omega}\cdot\nabla\psi\left(\bar{r},E,\hat{\Omega}\right)=$$

$$\int_0^\infty\int_{4\pi}d\hat{\Omega}'\sigma_s\left(\bar{r},E'\rightarrow E,\hat{\Omega}'\rightarrow\hat{\Omega}\right)\psi\left(\bar{r},E',\hat{\Omega}'\right)\qquad(1)$$

$$+S\left(\bar{r},E,\hat{\Omega}\right)$$

The first term to the left side describes the total collisions. The second term on the left side describes the particle streaming component, which is the directional derivative of the angular flux. The directional derivative generalizes the notion of a partial derivative, in which the rate of change of angular flux is considered along coordinate curves, such as x, y, z for Cartesian coordinates. This is implemented in the multi-group form of the LBE given in Equation (3). The first term to the right side is the net scattering component, which involves a fairly complex treatment with an associated differential scattering cross section. The second term to the right side is the source term, which is the simplest term to model, especially if the photon source is well-characterized and known as a function of position, energy, and direction.

Commonly, the transport equation is recast in a transport operator H, in which the net scattering component is subtracted from both sides of Equation (1), and it characterizes a fixed source problem in the following form:

$$H\psi = S_{\text{fixed}}\qquad(2)$$

3.1.2 Discrete Ordinates Formulation of the Linear Transport Equation

As developed by Carlson in 1958 (Carlson and Bell 1958), the angular flux (angular domain) is discretized into a careful choice of discrete directions such that a function can be evaluated at discrete points on a surface. Then, flux moments are preserved with quadrature integration over the discrete set of points. The spatial domain is handled by forming finite difference relationships based on the Boltzmann equation to evaluate the streaming.

3.1.3 Multi-group Application of the Linear Boltzmann Equation

The generalized multi-group LBE in 3D Cartesian coordinates is provided below:

$$\left(\mu\frac{\partial}{\partial x}+\eta\frac{\partial}{\partial y}+\xi\frac{\partial}{\partial z}\right)\psi_g\left(x,y,z,\mu,\varphi\right)+\sigma_g\left(x,y,z\right)\psi_g\left(x,y,z,\mu,\varphi\right)=$$

$$\sum_{g'=1}^{G}\sum_{l=1}^{L}\left(2l+1\right)\sigma_{s,g'\to g,l}\left(x,y,z\right)\left\{\begin{array}{l}P_l\left(\mu\right)\phi_{g',l}\left(x,y,z\right)+2\sum_{k=1}^{l}\frac{\left(l-k\right)!}{\left(l+k\right)!}P_l^k\left(\mu\right)\cdot\\\left[\phi_{C\,g',l}^{k}\left(x,y,z\right)\cos\left(k\varphi\right)+\phi_{S\,g',l}^{k}\left(x,y,z\right)\sin\left(k\varphi\right)\right]\end{array}\right\} \quad (3)$$

$$+S_g^{\text{fixed}}\left(x,y,z,\mu,\varphi\right)$$

where the triplet $\left(\mu,\eta,\xi\right)$ represents the three direction cosines, the triplet $\left(x,y,z\right)$ represents the 3D Cartesian coordinate position, and the doublet $\left(\mu=\cos\theta,\varphi\right)$ refers to the polar and azimuthal angles. The rest of the terms in Equation (3) are described in Table 1. The partial derivative terms are further simplified by using differencing schemes, which handles the spatial discretization of transport operator H (Sjoden 1997, Sjoden 2007, Yi 2007).

There are several observations in the application of Equation (3). For example, multi-group cross sections related to the physical problem are now required. In particular, a total cross section from groups 1 to G are needed, as well as the absorption cross sections and scattering cross sections with Legendre moments, with higher moments better treating anisotropic scattering behavior. For this thesis, Legendre order P_3 and higher are applied for photon transport to ensure sufficient scattering accuracy. In other words, one must consider the appropriateness of energy bin boundaries and number of bins necessary to capture the high fidelity afforded by the point-wise cross sections used by the Monte Carlo method. Multi-group

cross section generation then becomes an important tool to preserve proper photon transport physics.

The cross section libraries for Monte Carlo simulations using MCNP5/X/6 software use the ENDF6/7 cross sections; for deterministic transport with PENTRAN, CEPXS was used to generate photon multi-group cross sections for medical physics. Furthermore, in photon cross section generation, only downscattering cross sections were generated. This preserves one-way scattering physics in that only high-energy group photons can scatter into the low-energy groups.

Table 1: Discrete ordinates form of LBE terms defined.

Entity	Meaning or Expanded Definition
$P_l(\mu)$	l^{th} Legendre polynomial spanning 1 to Legendre Order L
$P_l^k(\mu)$	l^{th}, k^{th} associated Legendre polynomial
$\psi_g(x, y, z, \mu, \varphi)$	Angular flux for some group g
$\phi_{g',l}(x, y, z)$	l^{th} Legendre scalar moment for group g'
$\phi_{C\,g',l}(x, y, z)$	l^{th}, k^{th} cosine associated Legendre polynomial scalar flux moment for group g'
$\phi_{S\,g',l}(x, y, z)$	l^{th}, k^{th} sine associated Legendre polynomial scalar flux moment for group g'
σ_g	Total group macroscopic cross section
$\sigma_{s,g'\to g,l}$	l^{th} moment of the scattering cross section from g' into g
$S_g^{fixed}(x, y, z, \mu, \varphi)$	External source term at position (x, y, z) and direction (μ, φ)
$\phi_{g',l}(x, y, z)$	Flux moment which expands to (Relation A): $$\int_{-1}^{1} \frac{d\mu'}{2} P_l^k(\mu) \int_0^{2\pi} \frac{d\varphi'}{2\pi} \psi_{g'}(x, y, z, \mu', \varphi')$$
$\phi_{C\,g',l}(x, y, z)$	Flux moment which expands to (Relation B): $$\int_{-1}^{1} \frac{d\mu'}{2} P_l^k(\mu) \int_0^{2\pi} \frac{d\varphi'}{2\pi} \cos(k\varphi') \psi_{g'}(x, y, z, \mu', \varphi')$$
$\phi_{S\,g',l}(x, y, z)$	Flux moment which expands to (Relation C): $$\int_{-1}^{1} \frac{d\mu'}{2} P_l^k(\mu) \int_0^{2\pi} \frac{d\varphi'}{2\pi} \sin(k\varphi') \psi_{g'}(x, y, z, \mu', \varphi')$$

3.1.4 Advances in 3D Quadrature and the Quadratures Used

An improvement to 3D quadratures is a significant research topic and too broad for the thesis scope. It is important to identify the quadratures used in this thesis. The majority of computations used Legendre-Chebyshev (Pn-Tn) quadrature as is included in the PENTRAN software (Sjoden and Haghighat 1997, Longoni 2004).

In an initial thesis effort, the author contributed to prior research (Manalo, Yi et al. 2013) in identifying fixed source term modeling using Ahren's and Beylkin's Icosahedral quadratures (Ahrens and Beylkin 2009). Ultimately, because of the overhead costs in memory that were not optimized in the PENTRAN code, the more accurate Icosahedral quadratures were not considered for use in 3D deterministic transport modeling for medical physics applications. However, it should be mentioned that using Icosahedral quadratures significantly reduces the ray-effects for anisotropic sources, as linear accelerator head modeling particles are composed of highly forward peaked bremsstrahlung photon beams. An illustration of ray mitigation using the Icosahedral quadratures with a periodic boundary fixed source problem is shown in Figure 1.

(a) 192 pt IC   (b) 432 pt IC   (c) 672 pt IC   (d) 1032 pt IC
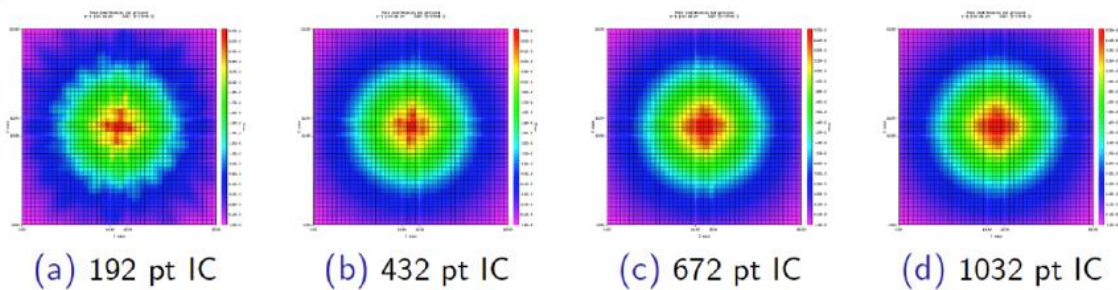
Figure 1. The ray mitigation with icosahedral quadratures.

In PENTRAN, the primary quadratures are the level-symmetric (the lower order) and Pn-Tn quadratures (the higher order). The Pn-Tn quadratures are of considerable interest for anisotropic problems, for example, a beam source and photon scattering in water and tissue phantoms.

A 3D quadrature is a set of directions and the corresponding weights allowing for effective numeric volumetric integration. For the discrete ordinates method, the 'N' in S_N indicates a discrete number of directions per octant, which is $N(N+2)/8$. For example, Figure 2 defines S_8 level-symmetric quadrature with 10 ordinates per octant (with associated level-symmetric weights not listed). Primarily, the legacy 3D quadrature in use is the level-symmetric quadrature, which has positive weights until S_{20}. While there are methods to extend the level-symmetric quadrature strategy, PENTRAN incorporates the use of Pn-Tn quadrature as the default quadrature above S_{20}, in which polar angles are set equal to Legendre polynomials of order N and azimuthal angles are determined by solving for roots of Chebyshev polynomials (Longoni 2004). The spatial directions of the Pn-Tn quadrature for S_{20} are provided in Figure 3.
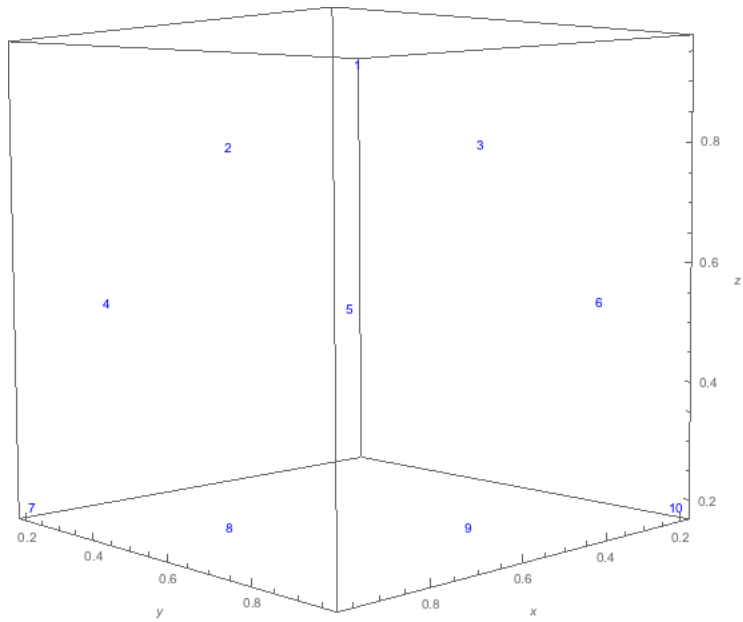
Figure 2. The S_8 level-symmetric quadrature in one octant.
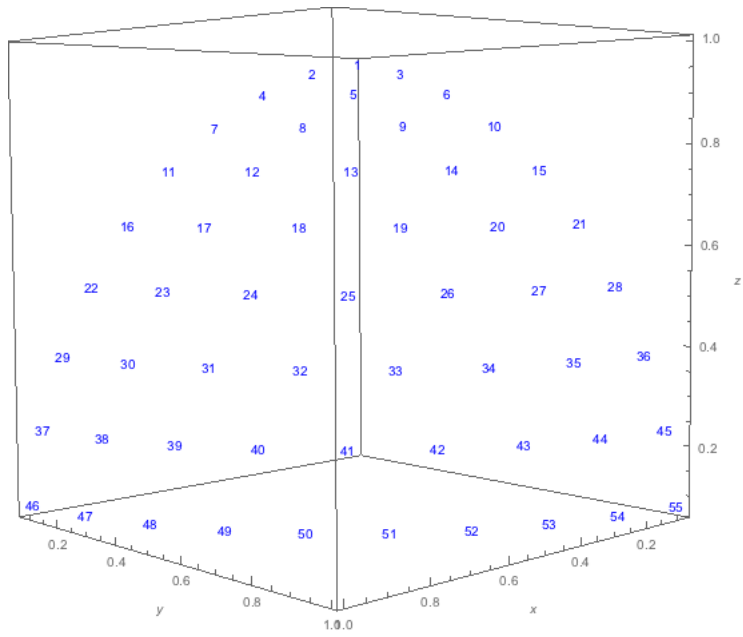
Figure 3. The S_{20} Pn-Tn quadrature in one octant.

3.2 Modeling the Linear Accelerator Head Model for Use in S_N Transport

The EDK-S_N method was adapted to a full Monte Carlo linear accelerator head model using phase space information for the Varian Clinac. This is an improvement over the previously applied step source approach. The EDK-S_N method was used to compute in-field and out-of-field dose, which will be presented in Chapter 4.

3.2.1 Linear Accelerator Discrete Energy Spectrum Modeling

Figures 4 and 5 show the 6-MV and 18-MV spectra obtained from commissioned Eclipse treatment planning system data for Georgia Tech's Clinac iX. The graphed spectra demonstrate the discretization of 16 and 40 energy transport groups (results generated by Mathematica). The 16 group and 40 group structures were analyzed to provide a reasonable matchup between the discrete probability density function (PDF) and to the continuous PDF; furthermore, they were selected to provide a convenient parallel decomposition choice as the factor of 4 is compatible with parallel CPU architecture in that CPUs for research were 16-core CPUs per socket. A goal for deterministic transport modeling has been to minimize the number of multi-groups while preserving accuracy. A more refined spatial spectrum method will be discussed in Chapter 4. The 6 MV and 18 MV spectra were initially used in a shielding study by author provided in Appendix A. However, because they are the simplified uniformly space distributed photon spectrum source terms, it does not correctly represent the real Linac head particle information including particle angles and magnitude. A more detailed full phase space particle information including spatial intensity map was obtained using Varian phase space information discussed in Chapter 5. Only the 6MV Linac is used, due to the neuron contamination for the 18MV Linac (Vanhavere, Huyskens et al. 2004).
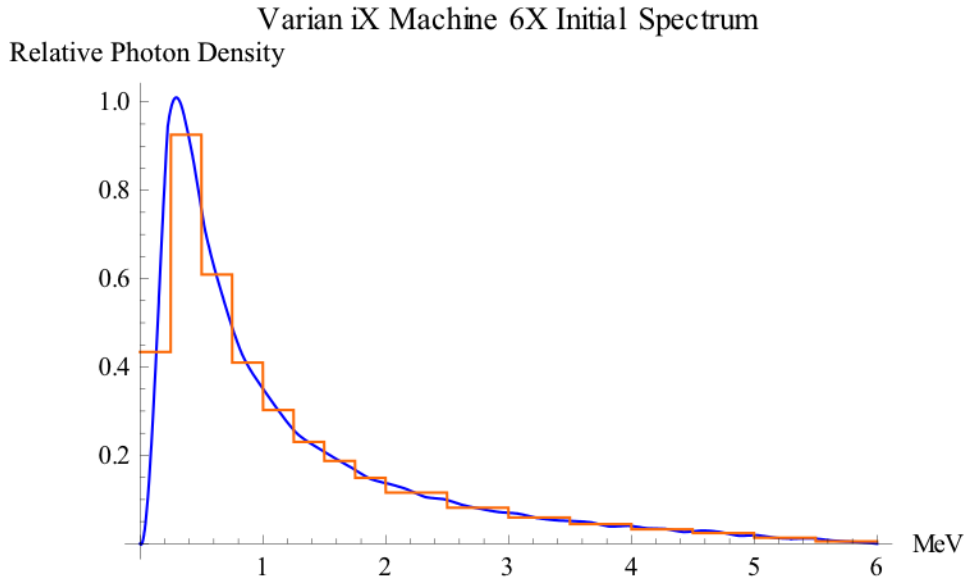
Figure 4. The 6-MV Linac head spectra obtained from commissioned Eclipse treatment planning system data for Georgia Tech's Clinac iX. The continuous spectrum is shown in blue line, the discretized histogram is shown in red line with 0.25 MeV per energy group up to 2 MeV and 0.5 MeV per group from 2 to 6 MeV, which makes a total of 16 energy groups.
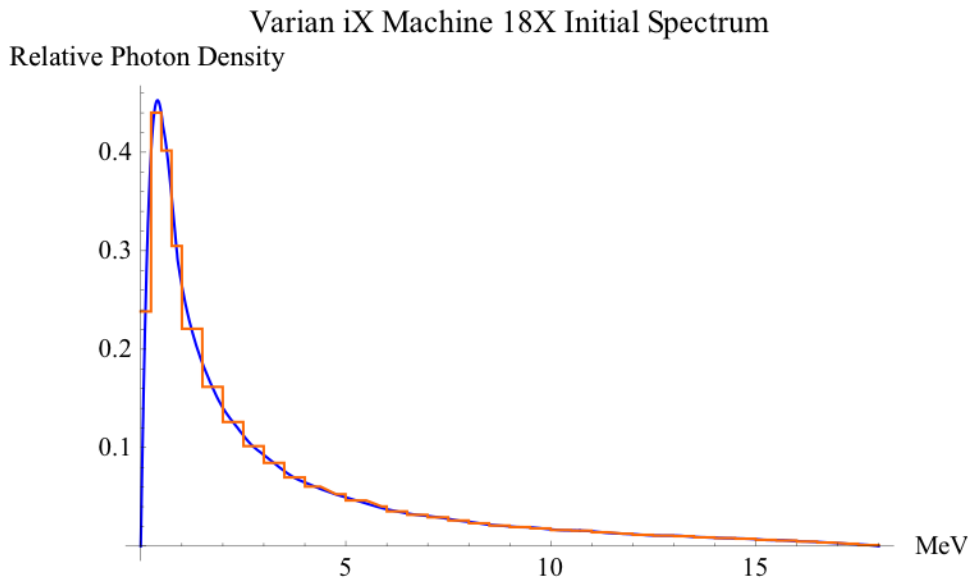
Figure 5. The 18-MV Linac head spectra obtained from commissioned Eclipse treatment planning system data for Georgia Tech's Clinac iX. The continuous spectrum is shown in blue line, the discretized histogram is shown in red line with 0.25 MeV per energy group up to 2 MeV and 0.5 MeV per group from 2 to 18 MeV, which makes a total of 40 energy groups.

These illustrations show that 16 energy groups and 40 energy groups are respectively handled using the multi-group method in the PENTRAN transport calculation system. 1,2,4,8 or 40 CPUs can decompose each group individually and simultaneously. Each energy group will report photon flux at the end of the calculation. The dose calculation are implemented based on the photon results coupled to the Monte Carlo generated electron dose kernels (described in Chapter 4) on either a 1 cm or 0.5 cm grid with a semi-conformal adaptive dose map.

3.2.2 Discrete Spacing Model and Resolution: Angular Considerations for Source Modeling

Before attempting to apply a phase space to discrete ordinates transport method, a simple phantom problem was designed with a simple cone source at 100 SSD and a 40 cm x 40 cm x 40 cm water phantom. The field size is a 10 cm x 10 cm at the isocenter. To approximate the directional source behavior, an isotropic source was collimated to a cone source with an angle opening of 5.72 degrees. As shown in Figure 6(a), the entire space, including source, air, and water, was discretized with 1 cm x 2 cm x 2 cm grids in air and 1 cm x 1 cm x 1 cm grids in water. As shown in Figure 6(b), the photon beam source is a 10 cm x 10 cm surface source, which was projected into the water phantom.
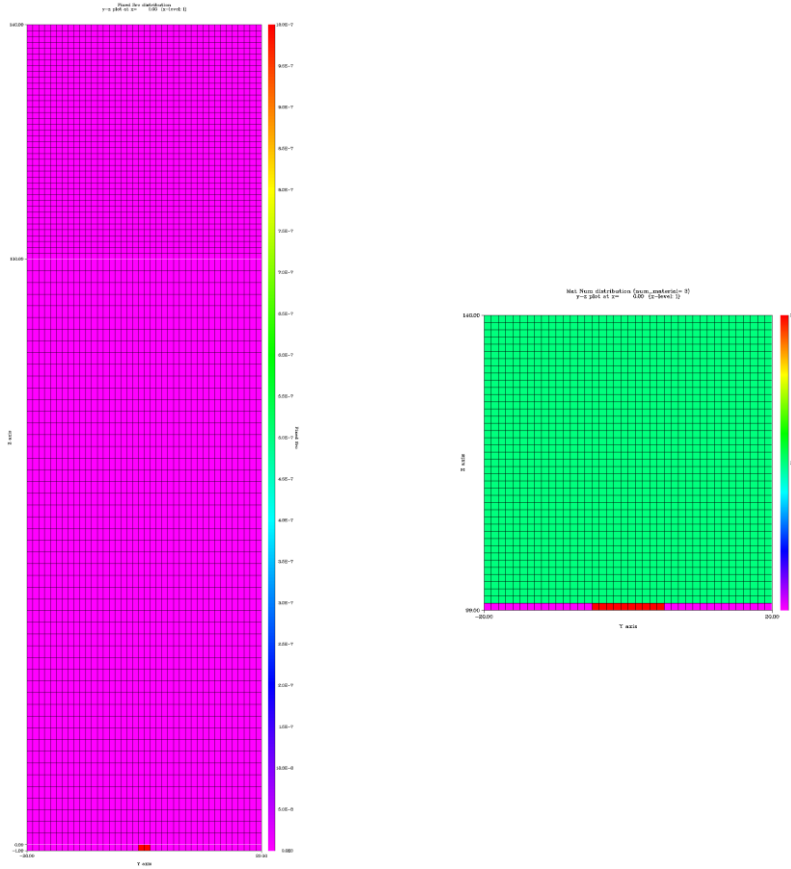
Figure 6. Spatial discretization of the photon source: (a) SSD Point Source (Red Point on Bottom of Purple Surface), and (b) 10cm x 10cm surface source facing the water phantom.

3.2.3 Discrete Ordinates Splitting Modeling and Ray Effect

The following S_N orders in the transport model were evaluated: 20, 32, 40, 50, 62, and 100. Figures 7-9 show the progression of quadratures from S_{32}, S_{50}, and S_{100}. Only when the S_N order is higher than 50, will the discrete angles have at least one directional cosine along the +z axis (the photon penetrating direction) less than the 2.86 degree cone source, which corresponds to the 10 cm x 10 cm field at the water phantom surface with SSD = 100 cm. The effect of this quadrature modeling is shown in Figure 10.

The initial attempt was to apply hybrid calculations using a version of PENTRAN, termed PENTRAN-CRT, which includes both the S_N and the method of characteristics (MOC).

More specifically, a user is able to select a transport method on a coarse mesh basis: S_N or MOC. The calculations using S_{62} resulted in severe ray effects, in that the photon fluence is only calculated along discrete angular ordinates in the +z direction, especially with the MOC ray tracing transport method. As a result, the EDK-S_N was pursued using only S_N transport (not MOC) inside each coarse mesh, with the source mapped directly onto a coarse mesh surface.

The S_{62} Pn-Tn quadrature was generally applied for the EDK-S_N. Figure 11 shows that a single spatial energy PDF at a point source, transported using MOC is not sufficient for transport accuracy, and thus dose accuracy. Accurate source terms must then be modeled providing large enough surface mesh to mitigate any source-based ray effects. Ray effects in 3D S_N are always present regardless of quadrature choice as this is a function of the hyperbolic nature of the streaming operator (Lathrop 1968), but they can be mitigated with increasing ordinate resolution. The choice in quadrature order is a trade-off between maximal accuracy and computation time.
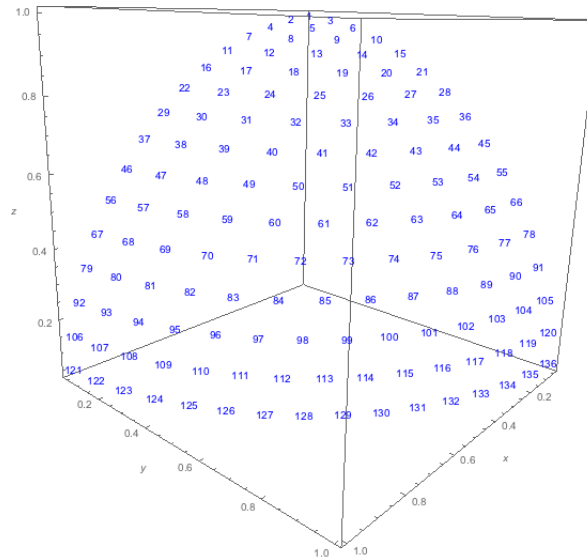
Figure 7. Pn-Tn S_{32} (136 angles per octant).
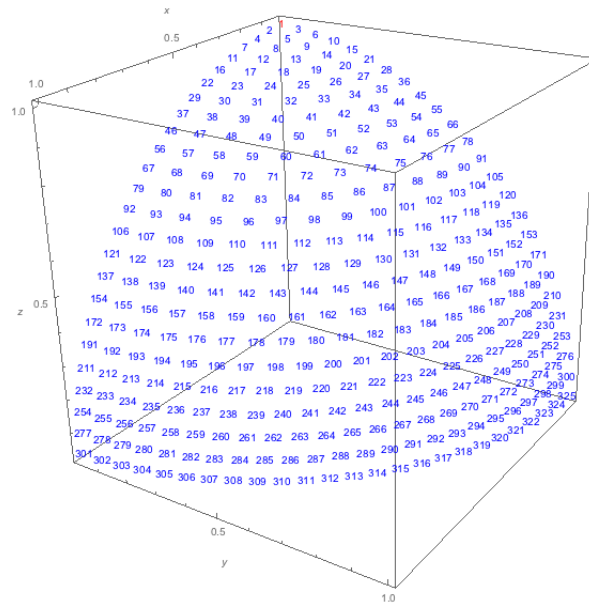
Figure 8. Pn-Tn S_{50} (325 angles per octant).
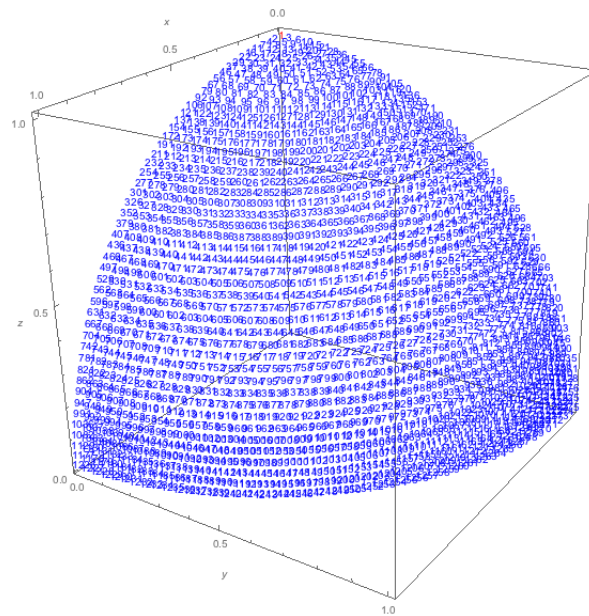
Figure 9. Pn-Tn S_{100} (1275 angles per octant).
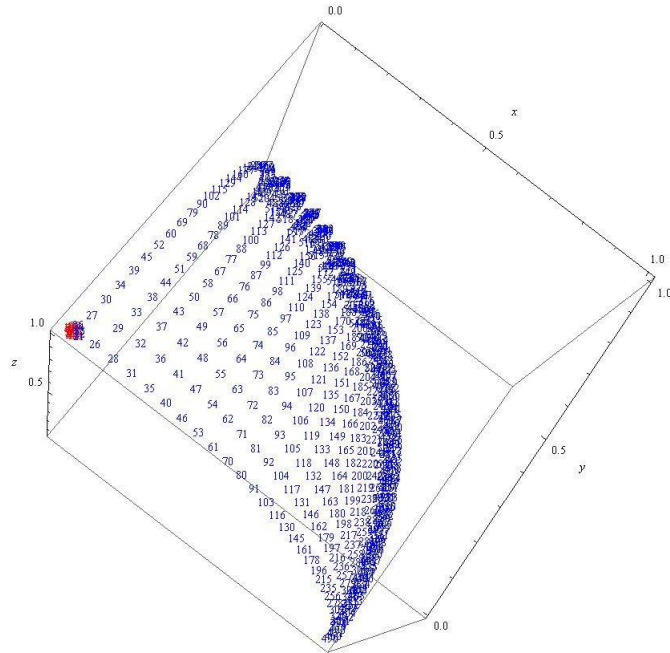
Figure 10. Discrete angle splitting using Pn-Tn S_{62}.
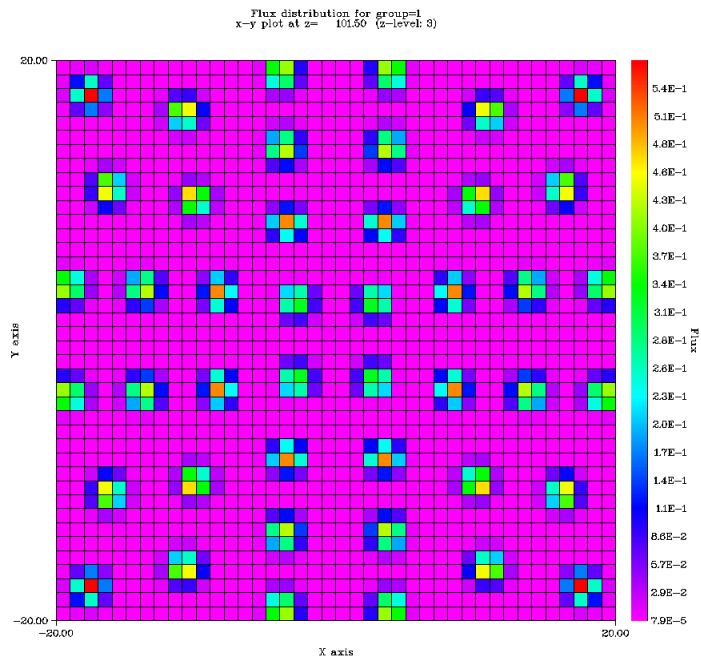
Figure 11. An example of significant ray effects in angular sources with the MOC.

24

3.3 Georgia Tech Varian Clinac

This section provides a brief introduction to Georgia Tech's Varian Linear Accelerator as some results of the thesis will be compared with the golden beam data obtained using the Clinac's associated treatment planning system.

3.3.1 Georgia Tech Varian Clinac

In 2012, a Varian Clinac iX Linear Accelerator (VCLA) was installed in Boggs Building at Georgia Tech as part of the NRE/MP Program in the new Radiological Science and Engineering Laboratory (RSEL). The VCLA vault was designed according to NCRP 151 (NCRP 2005), with surrounding shielding materials and thicknesses of the Clinac room, shown in Figure 49 in Appendix A. The 4-feet-thick primary wall concrete is listed as wall A and B1, and the 2-feet-thick secondary wall of high density concrete is indicated by walls C and D1 (McGinley 2011).

Appendix A discusses the development of suitable multi-group cross sections for discrete ordinates (S_N) transport simulations of the vault using 6 MV and 18 MV Clinac source spectra. The radiation transport forward-adjoint technique is applied to assess shielding effectiveness, and to benchmark the results with clinical measurements and Monte Carlo (MC) simulations.
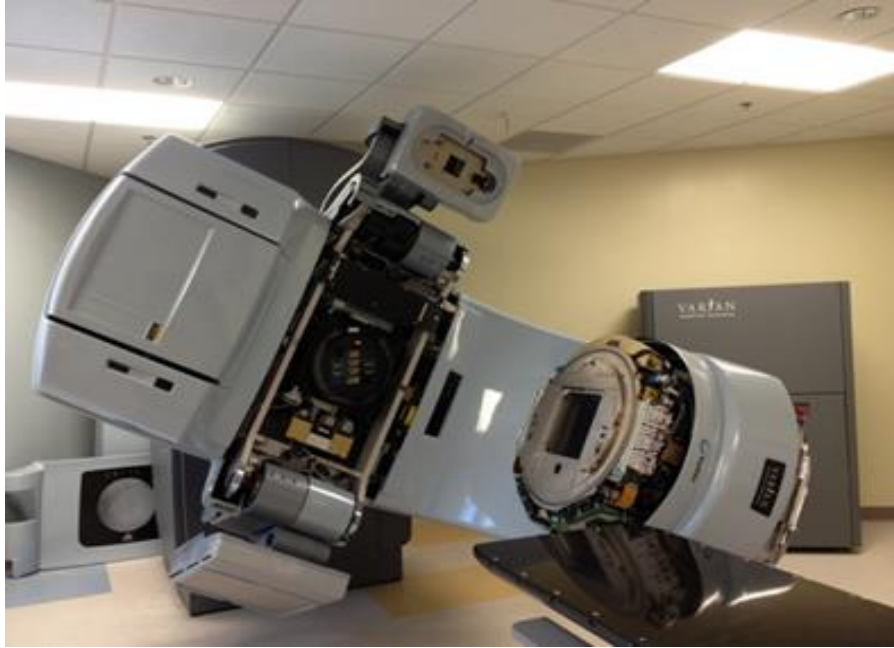
Figure 12. The Varian Clinac iX Linear Accelerator located in the basement of Boggs Building at Georgia Tech.

CHAPTER 4

MONTE CARLO - ELECTRON DOSE KERNELS (EDK) GENERATION

AND S_N TRANSPORT FLUX COUPLING

This chapter discusses the important elements in hybrid coupling of Monte Carlo-based

EDK to deterministic transport driving a solution for absorbed dose distribution in a water

phantom. Also, a discussion is included on the need for accurate source terms and comparison of

the relative dose in a water phantom obtained with MCNP and PENTRAN. Figure 13 is a

visualization of the Varian phase space of the photon source terms that can be applied to both

MCNP and PENTRAN for use in a dose calculation in a water phantom. The photon flux spatial

intensity distribution map, which was generated using Matlab, generated by extracting each

particle information from the Varian phase space data for a 6MV, 10cm by 10cm field size, is

illustrated below.
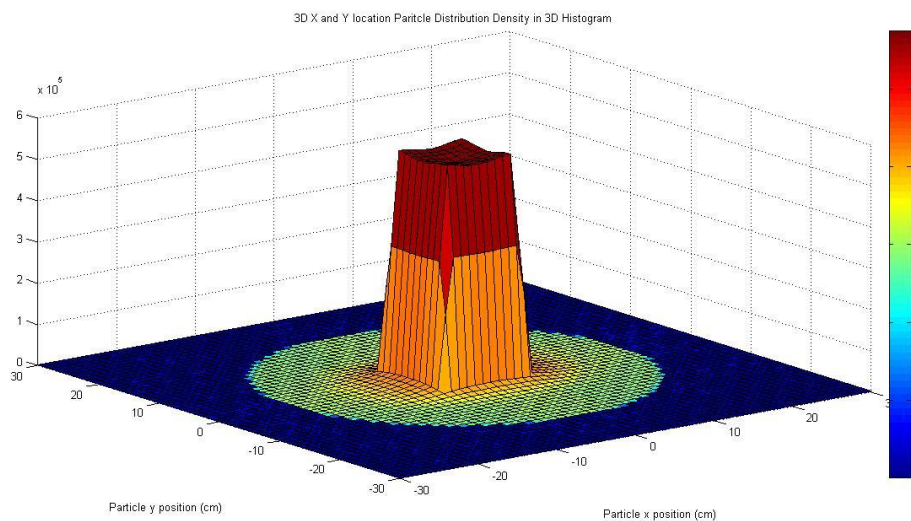
Figure 13. The 3D contour of phase space of the photon source terms that are applied to S_N method for driving EDK.

<center>**4.1 Electron Dose Kernels**</center>

This section provides two forms of the EDK method: a generalized EDK formulation, and a detailed step-by-step methodology with noted improvements in application of EDK-S_N.

4.1.1 General EDK-S_N Formulation in PENTRAN

The EDK-S_N method, or "electron dose kernel-discrete ordinates method" was developed to calculate voxelized organ doses in the human body principally for applications in high-energy external photon beam therapy. The initial computational approach was proposed by G. Sjoden et. al.(Al-Basheer, Sjoden et al. 2009). This thesis used a simple, hypothetical flat MV source that was later improved and expanded (Huang, Sjoden et al. 2009, Huang, Sjoden et al. 2010)

The initial work of the EDK-S_N method was tested with an 8 MV flat photon beam source directed at the middle anterior of a 15-year old male phantom, and the results were found to agree with Monte Carlo results in a homogenous phantom to within 10% in far out-of-field regions (Al Basheer 2008) except in strongly heterogeneous regions, where it became difficult to validate the accuracy of the Monte Carlo, compounded by the often significant inherent uncertainties in the stochastic simulations (Knöös, Wieslander et al. 2006, Fogliata, Vanetti et al. 2007). The EDK-S_N method was demonstrated using CT-based voxelized anatomical patient phantoms and calibration phantoms. It has been shown that the EDK-S_N method can be an order of magnitude faster than Monte Carlo simulations for whole body dose (Al-Basheer, Sjoden et al. 2009, Huang, Sjoden et al. 2009, Huang, Sjoden et al. 2010).

To begin the EDK-S_N procedure, one first rapidly solves for the photon transport deterministically over the entire phase space of the phantom using 3D discrete ordinates method with PENTRAN on parallel computers. In this step, discretization of a phantom is performed as required among the energy, angle, and spatial variables using parallel computation for rapid

<center>28</center>

global solution. The *photon net current* in each Cartesian voxel is derived from the solution of the Boltzmann equation. At the end of this step, the photon flux, photon current, and net current vector direction are determined spanning the phase space of the phantom or CT dataset, as appropriate. Then, this highly detailed angular discrete data, rendered globally, is used to project the absorbed dose and map it into the surrounding voxels. The final absorbed dose is calculated by summing on a mesh by mesh basis, scaled by the magnitude of the photon fluence, using the electron dose kernels (EDKs). Fine mesh scalar fluxes are not considered as they do not provide a directional component. A flowchart is provided in Figure 14 to describe the dose calculation flow, including the EDK-S_N 3D dose computation system and the full Monte Carlo 3D dose computation, which will be introduced in the following sections.
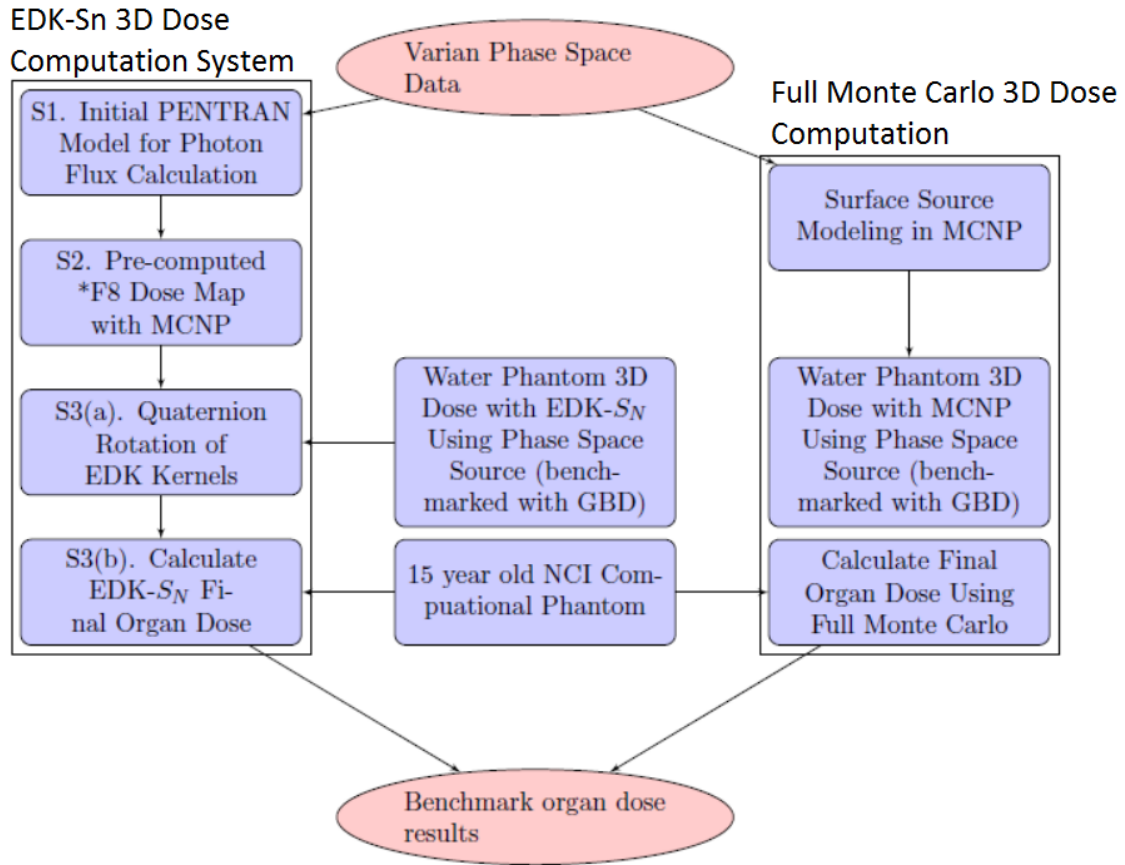
Figure 14. A flowchart describing the EDK-S_N process and Full Monte Carlo process in order to obtain 3D dose.

4.1.2 Advancement of the EDK-S_N Method

This section provides additional discussion on the advancement of the EDK-S_N method. The method employs CT-based voxelized anatomical patient phantoms, and the absorbed doses are computed in three steps described below.

Deterministic discrete ordinates calculations of the photon transport equation are performed with discretization of the energy, angle, and space variables. In steady state, the multi-energy group transport equation is described by Equation (3) in Section 3.1.3.

The photon net current is derived from the solution of the transport equation. At the end of this step, the photon current, including flux and direction, will be calculated everywhere inside of the phantom or CT dataset.

For any S_N calculation, the PENTRAN code preserves angular information explicitly in scalable parallel-stored local arrays. The total net current is represented by $\vec{J}_{net}$, which is composed of J_{nx}, J_{ny}, and J_{nz} in Cartesian coordinates along x, y and z shown by Equation (1). J_{nx}, J_{ny}, and J_{nz} are the net components of partial currents along each axis, as shown by Equation (2). $\hat{j}_u$ is the unit vector of the total net current $\vec{J}_{net}$ for a specific voxel, as shown by Equation (3). Solving the Boltzmann transport equation enables direct calculation of $\vec{J}_{net}$ from angular flux for each voxel in 3D.

$$\vec{J}_{net} = J_{nx}\hat{i} + J_{ny}\hat{j} + J_{nz}\hat{k} \tag{1}$$

$$\begin{aligned} J_{nx} &= J^+_{nx} - J^-_{nx} \\ J_{ny} &= J^+_{ny} - J^-_{ny} \\ J_{nz} &= J^+_{nz} - J^-_{nz} \end{aligned} \tag{2}$$

$$\hat{j}_u = \frac{\vec{J}_{net}}{\left|\vec{J}_{net}\right|} \tag{3}$$

In this step, the highly detailed angular data rendered globally over the phantom from the S_N solution is used to project the dose and map it to surrounding voxels; the dose is accumulated on a mesh by mesh basis, scaled by the magnitude of the photon fluence, using the Electron Dose Kernels (EDKs). The EDKs are pre-computed using full physics charged particle Monte Carlo electron transport for a single monoenergetic pencil photon beam in either soft tissue, bone, or lung tissue, and adapted to any direction on the unit sphere so as to enable coupling to photons traveling in any direction determined via the S_N calculations.

The electron dose kernel fraction in distal voxels (i,j,k) due to a primary photon at (i',j',k') can be determined in terms of the initial photon energy for a particular energy group. Figure 15 shows a schematic of photons in a 'dose-driving voxel' (DDV) at location (i',j',k') creating charged particles and energy deposition in voxels distal from the DDV. By partitioning the energy deposited in voxel (i, j, k), into multiple energy bins aliased to the S_N multi-group energy structure, the fractional electron dose kernel contribution per unit photon flux per source particle in the forwardly peaked current direction can be constructed. A partial MCNP input deck is provided Appendix B.
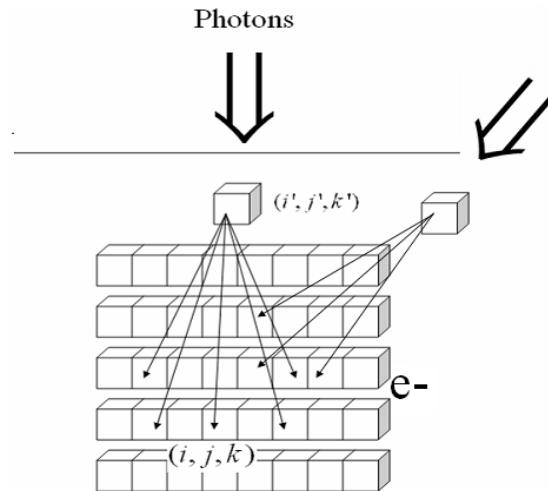
Figure 15. A schematic of photons in a 'dose driving voxel' (DDV) at location (i',j',k') creating charged particles and energy deposition in voxels distal from the DDV.

Figure 16 shows the MCNP generated electron dose kernel for a 0.5 cm x 0.5 cm x 0.5 cm for a

0.5 MeV energy bin. The dose kernel in each energy group will be rotated along the $\hat{j}_u$ direction

in step 3.
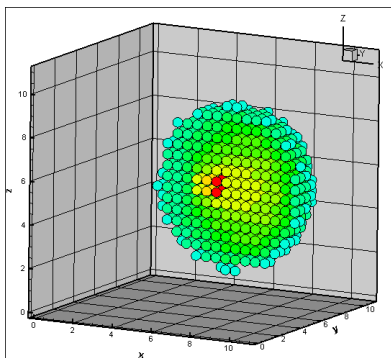
Figure 16. An illustration of the 3D EDK Dose kernel (cross-sectional view) in water. The dose kernel is pre-calculated for each energy group, and pre-stored for any photon current-driven rotations.

4.1.2.3 Step 3

The final step involves rotating the EDK kernel using quaternion rotation, and projecting

the EDK kernels along the photon current direction, for each energy group, and then summing up

33

to obtain the absorbed dose for each voxel. The rotation is necessary because the dose kernel was initially generated along a positive z-axis, but for each voxel there is a different photon current direction. In each voxel, the kernel needs to rotate along the photon current direction prior to summation across energy group contributions. The absorbed dose for voxel (i,j,k) can be expressed as:

$$D(i,j,k) = \sum_g \left(\sum_g EDF_g(i,j,k)_S \right) \left(\phi(i,j,k)_{S_N g} \right) \beta / M(i,j,k) \qquad (4)$$

where $EDF_g(i,j,k)$ is the electron dose kernel fraction in group g, β is the photon normalization factor, $\phi(i,j,k)_{S_N g}$ is the scalar flux, and $M(i,j,k)$ is the mass of the voxel. The normalization factor β is dependent on the mesh size.

In this subsection, quaternion rotations on EDK dose kernel along direction $\hat{j}_u$, with

magnitude $\left|\vec{J}_{net}\right|$ were implemented, improving on prior application of Euler rotation for

EDK-S$_N$. Figure 17 illustrates the EDK kernel rotation.
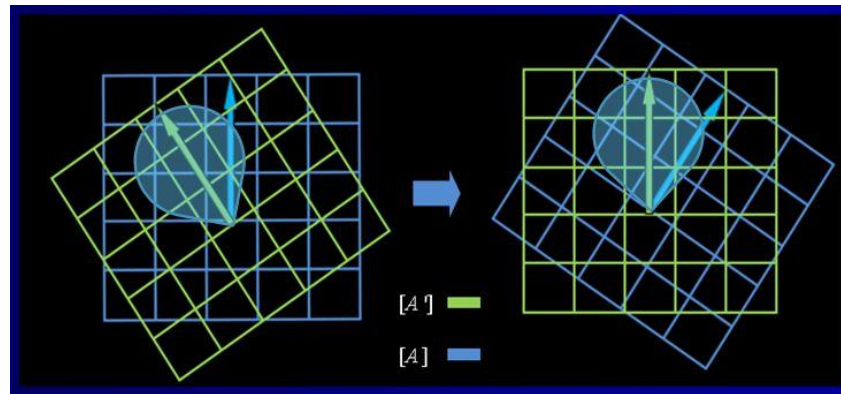
Figure 17. EDK rotation from grid A into A'.

By using quaternion rotation to rotate electron dose kernel, in particular rotating

pre-computed EDKs along the quaternion, enables projection dose to the appropriate 3D voxel.

Using quaternion rotation not only improves speed over the Euler angle rotation method, it also

avoids the problem of gimbal lock. This rotation algorithm improved storage, and provided a

faster rotation calculation for the EDK kernel. In particular, the older Euler angle representation,

as the old method pre-stored rotations in files, making it necessary to read a file for each rotation

performed.

4.1.2.5 Quaternion Rotation and Application to EDK

This section describes the basics of the quaternion rotation and how the quaternion

rotation is applied to rotate EDK to $\vec{J}_{net}$. A diagram of quaternion rotation is shown in Figure 18.

Graphical representation of
quaternion units product as
90°-rotation in 4D-space

ij = k
ji = -k
ij = -ji
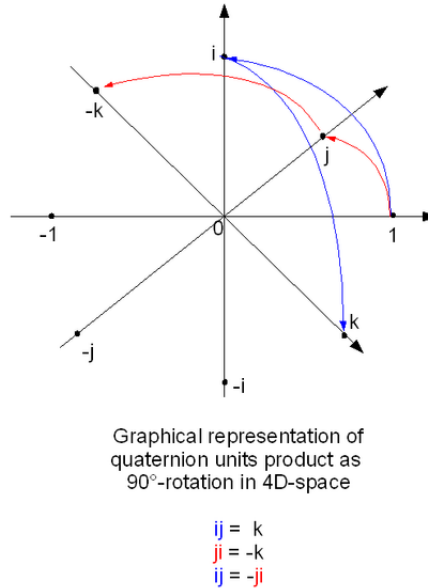
Figure 18. A diagram demonstrating a 90-degree quaternion rotation.

A rotation through an angle of α around the axis defined by a unit vector $\vec{u}$

$$\vec{u}=\left(u_x,u_y,u_z\right)=u_x\hat{i}+u_y\hat{j}+u_z\hat{k} \tag{5}$$

can be represented by a quaternion q. This can be performed using an extension of Euler's

formula shown in Equation (8). The point (w,x,y,z) represents a rotation around the axis directed

by the vector u(x,y,z) by an angle.

To summarize, any quaternion is an expression of Equation (6). The quaternion rotation

angle between the rotation axis and the new vector is indicated by Equation (7). The unit

quaternion q can be further written in terms of rotation angle as shown in Equation (8). The

resulting rotated vector $\vec{v}'$ can be obtained through Equation (9).

36

$$q = w + x\hat{i} + y\hat{j} + z\hat{k} \tag{6}$$

$$\alpha = 2\cos^{-1} w = 2\sin^{-1}\sqrt{x^2 + y^2 + z^2} \tag{7}$$

$$q = \cos(\alpha/2) + \vec{u}\sin(\alpha/2) \tag{8}$$

$$\vec{v}' = q\vec{v}q^{-1} = \left(\cos\frac{\alpha}{2} + \vec{u}\sin\frac{\alpha}{2}\right)\vec{v}\left(\cos\frac{\alpha}{2} - \vec{u}\sin\frac{\alpha}{2}\right) \tag{9}$$

Quaternions are analogous to an axis-angle rotation, and are numerically stable in prevention of an issue termed 'gimbal lock' which is the loss of a degree of freedom in 3D gimbal. Three components are space (x,y,z) , and the fourth component w is a rotational component. In the EDK kernel application, the dose position and magnitude are calculated upon rotating the kernel through the rotating axis of $\vec{J}_{net}$, through quaternion rotation.

The EDK-S_N method serves as a critical link in accumulating the absorbed dose in each fine mesh driven by fluence in the DDV. Accumulation of the dose in each voxel of tissue is possible because the accumulated dose in each voxel for each photon energy group is based on the S_N-computed photon flux which is then projected, due to electrons streaming along the photon current vector, derived from the S_N simulation. The EDK-S_N dose calculations were first performed for several slab phantoms using material specific absorbed dose kernels with 1 cm x 1 cm x 1 cm mesh size. This was later improved to a 0.5 cm x 0.5 cm x 0.5 cm mesh size. An example of this mesh improvement is shown in Figure 19. The goal for the EDK-S_N method would be to apply the same precision as a computational phantom with voxel sizing of 2 mm x 2 mm x 2 mm. The improvement to 5 mm is an additional refinement (this is the finest resolution given the computational resources available at Georgia Tech), which can better characterize volumetric detail and reduce ray effect; consider in Figure 18 the improvement in beam

resolution where the midline of the beam has a 'fatter' middle section of the beam, which is clearly not evident in using 1 cm meshes.
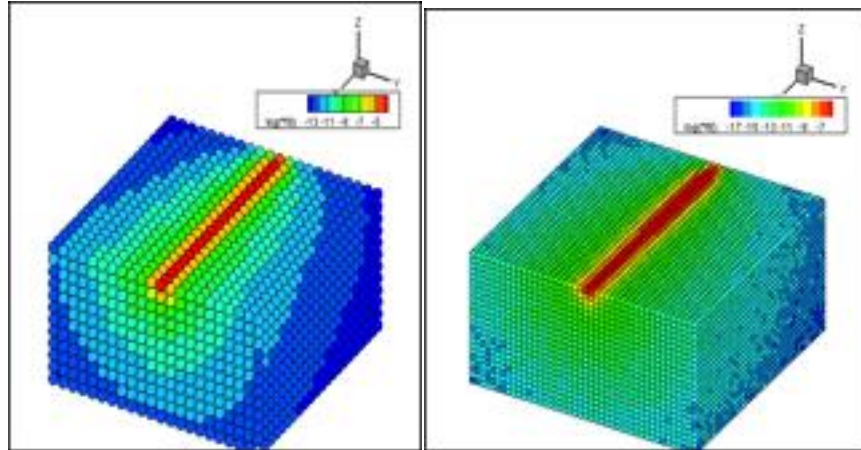
Figure 19. Total dose distribution on a $11\times11\times11\text{cm}^3$ water phantom with 1.0 cm meshes and 0.5 cm meshes.

4.2 Source Modeling for the EDK-S_N Method

A single probability distribution for energy was used in Chapter 3, when using a representative Clinac 6MV spectrum to serve as the effective source term for adjoint detector response modeling, as was seen with the probability distribution functions (PDFs) in Figure 4 and Figure 5. The gains in phase space accuracy are lost when reducing the phase space to a source having only a single energy spectrum. While a single PDF representation is acceptable for many-group photon cross section generation for shielding calculations (Appendix A as an example), more energy and space distributions are needed for the EDK-S_N dose application.

The challenge involves applying multiple spatial distributions to match the variation of the source term spatially, as a function of energy. To minimize computational burden, analysis was performed to consider suitable sampling for sufficient source term accuracy. This was done

by running 5 separate radial source problems within the PENTRAN code. The energy PDFs for radial rings of 0.5 cm segments were generated from the Varian phase space, and are shown in Figure 20. This figure represents a significant analysis accomplished by reading the data in Matlab, and programming a discretization of the source term to convert the phase space to ring distributions. Figure 20 shows the correct spectrum mapping in Monte Carlo and deterministic transport for spectrum modeling according to the Varian phase space information. The same figure also demonstrated the real phase space distribution in 3D histogram. According to the photon distribution, a five ring-shaped histogram has been computed and applied to Sn calculation. The ring radii consist of 0 cm to 0.5cm, 0.5cm to 1 cm, 1cm to 1.5 cm, 1.5 cm − 2 cm, and an outer ring; to simplify further the radius 2 cm (diameter 4 cm) to the rest of the 10 by 10 cm compose the same histogram. All S_N current results on these five rings are summed at the end. Figure 21 shows the application of the modeling of one of the five source rings.
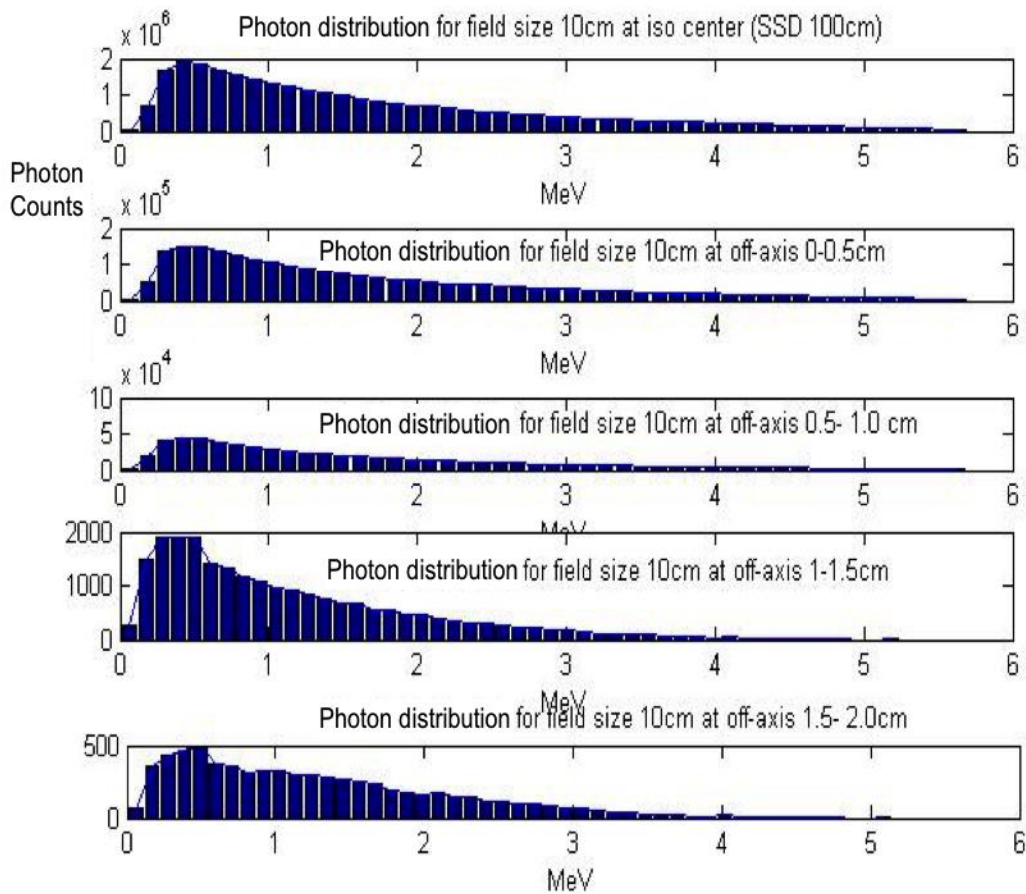
Figure 20. Photon distributions of phase space for 5 radial segments of the Varian phase space for S_N calculations.
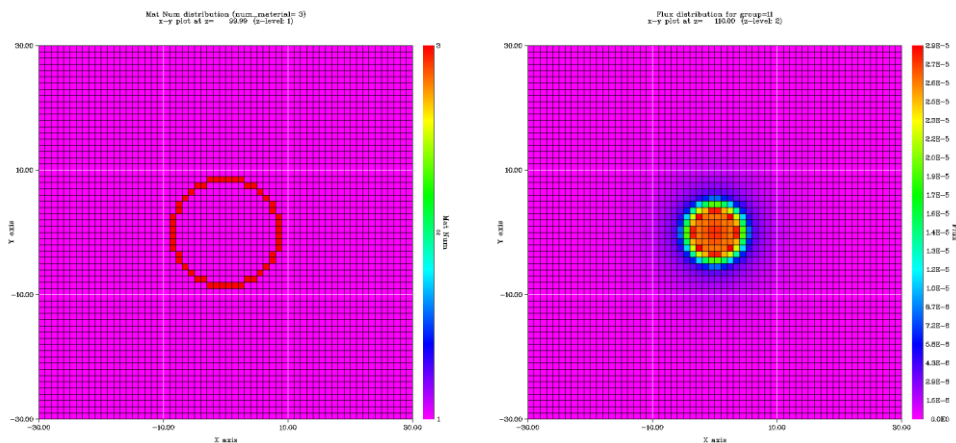
Figure 21. Modeling and results with S_N computation: (a) Ring source (1 of 5) (b) photon flux distribution at source plane in Group 1 (energy range 5.5 to 6.0 MeV).

4.2.1 EDK-S$_N$ Improvements in Accuracy with Realistic Source Term Modeling

It is important to show the improvements in using the Varian phase space data, which are qualified and benchmarked to the Varian measured representative golden beam data (GBD), over using a user-parameter driven source term with spectrums obtained from a TPS.

As an example, using the user-parameter driven source term method, percent depth dose curve was calculated using MCNP (normalized to maximum dose point) and compared to clinical chamber CC04 measurement comparison. A 6MV photon beam is incident into $60\times60\times60$ cm^3 water phantom, SSD setup at 90 cm, under different collimator field sizes 4×4 cm^2, 10×10 cm^2, and 30×30 cm^2 square field. The resulting tally vs. comparison is given in Figure 22 and errors are reported in Figure 23. The percent depth dose (PDD) errors were generally in the range of 5%, with some increase in error to 10% for the smallest field size. This level of accuracy was not sufficient within 5% dosimetric accuracy requirements for in-field clinical applications, with just the use of a Monte Carlo source term defined using SDEF within MCNP. These figures demonstrate the requirement to obtain a more accurate source term.

According to International Commission on Radiation Units and Measurements (ICRU), an ICRU report (Shalek 1977) recommended that the dose be delivered to within 5% of the prescribed dose in field. Considering the many steps involved in delivering dose to a target volume in a patient, each step must be performed with an accuracy to within 5% to achieve the ICRU recommendation (Kutcher, Coia et al. 1994). As achieved in the computation results, beyond the dose build-up region, the PDD deviation between MCNP simulation results with simplified 6MV monoenergetic spectrum will induce error more than 5% error for in-field dose beyond 15 cm depth in homogenous phantoms, even for standard 10 cm by 10 cm field size in Figure 22, compared to the real water phantom measurement (with IBA CC04 detectors);

Therefore, corrected phase space information for different locations, direction of the particles and spectrum must be corrected into the source modeling in EDK-S_N computation.

Photon flux distribution with 0.5 cm meshes as calculated using PENTRAN for a 6 MV clinical photon beam is represented by an equivalent cone source projected to the water block surface. There are 12 energy groups of 0.5 MeV bin width (highest energy in upper-left corner, lowest energy in lower-right corner). The smaller the field size should be accompanied with a higher S_N order. Figure 24 provides a 10 cm x 10 cm photon surface source calculation with the flux distribution in the 40cm x 40cm x 40 cm water phantom for a S_{20} deterministic transport calculation, and Figure 25 provides a flux distribution for S_{40} with smaller divergence angle. Figure 26 is a detailed local YZ view for one group, at a lower 1 cm resolution and some minor ray effects, which are mitigated further when using 0.5 cm meshes and a minimum of S_{40} quadrature.

Percent Depth Dose for water phantom(Monte Carlo calculation and clinical chamber measurement comparison) SSD at 90cm -6MV clinical photon beam
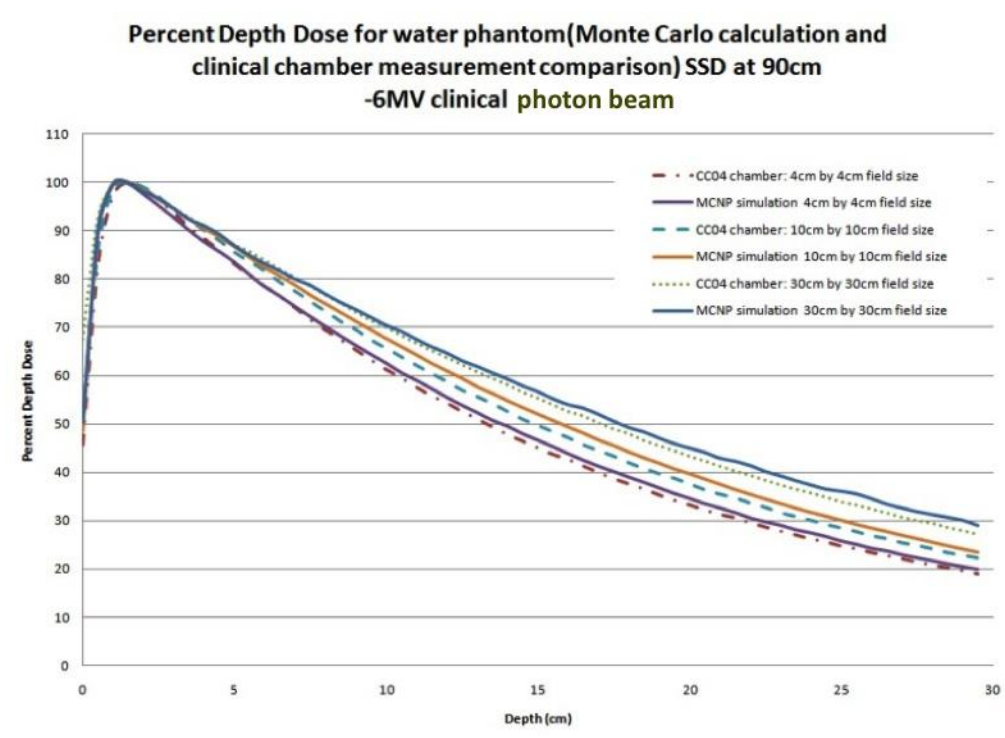
Figure 22. The PDD profiles obtained with Monte Carlo calculation using various simulated 6 MV beams based on the user-parameter driven source term method.

PDD calculation Percent Difference between Monte Carlo simulation and and clinical chamber measurement comparison-6MV clinical incident photon beam
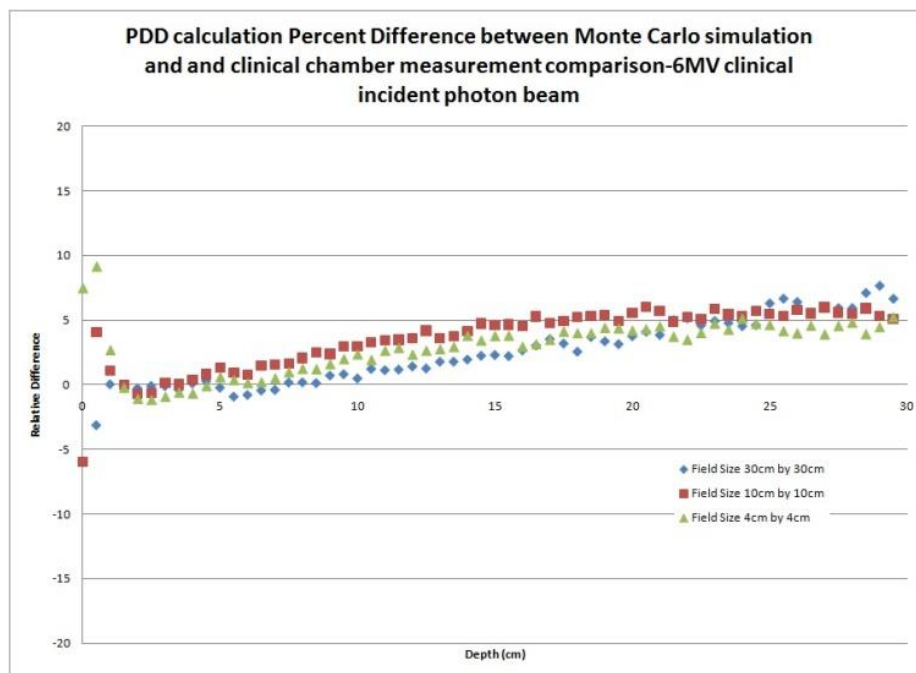
Figure 23. The percent differences between the PDD obtained with Monte Carlo calculations and the measured data for a 6-MV beam. The Monte Carlo calculations were based on the user-parameter driven source term method.
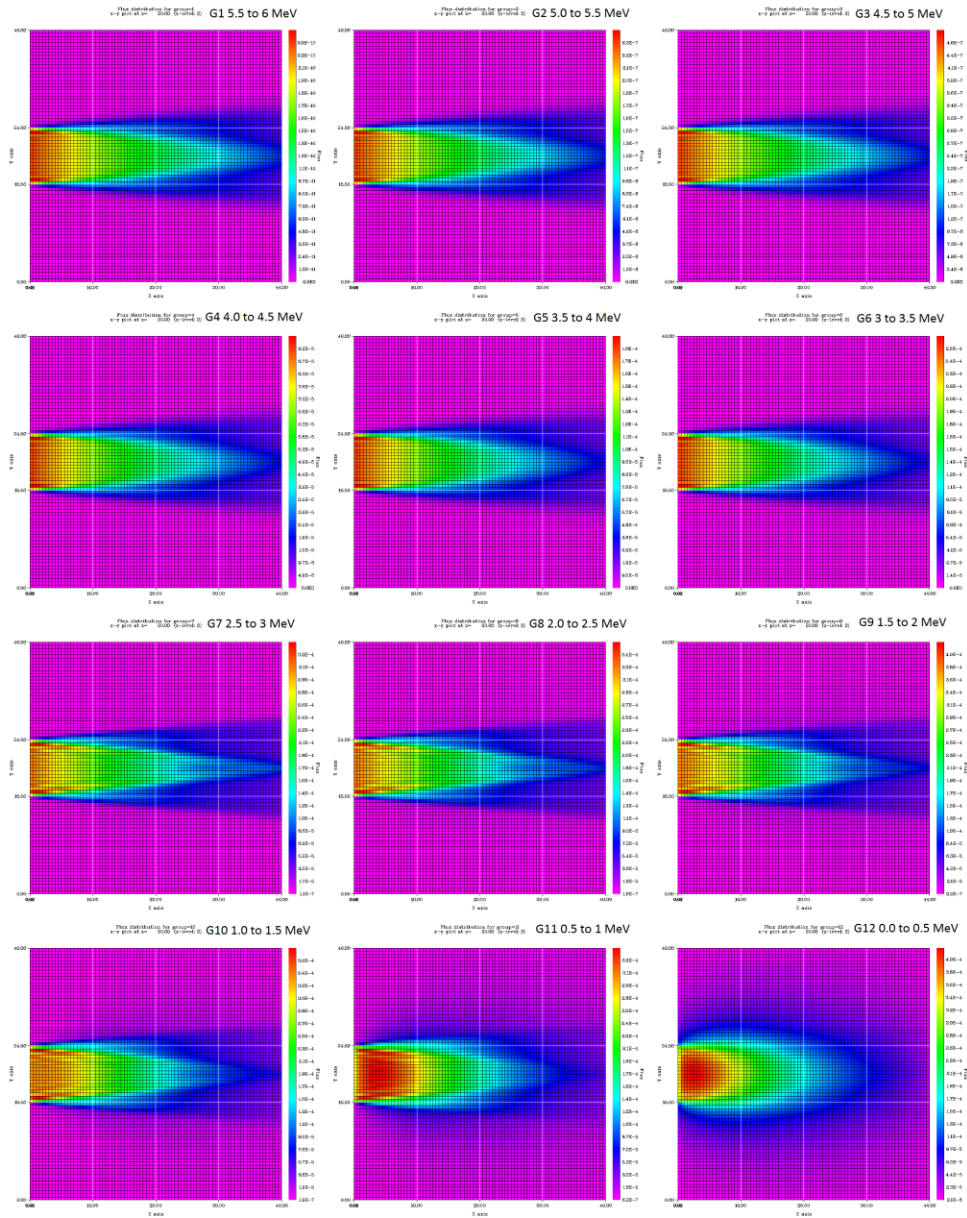
Figure 24. PENTRAN flux distribution using 0.5 cm mesh with S_{20} quadrature.
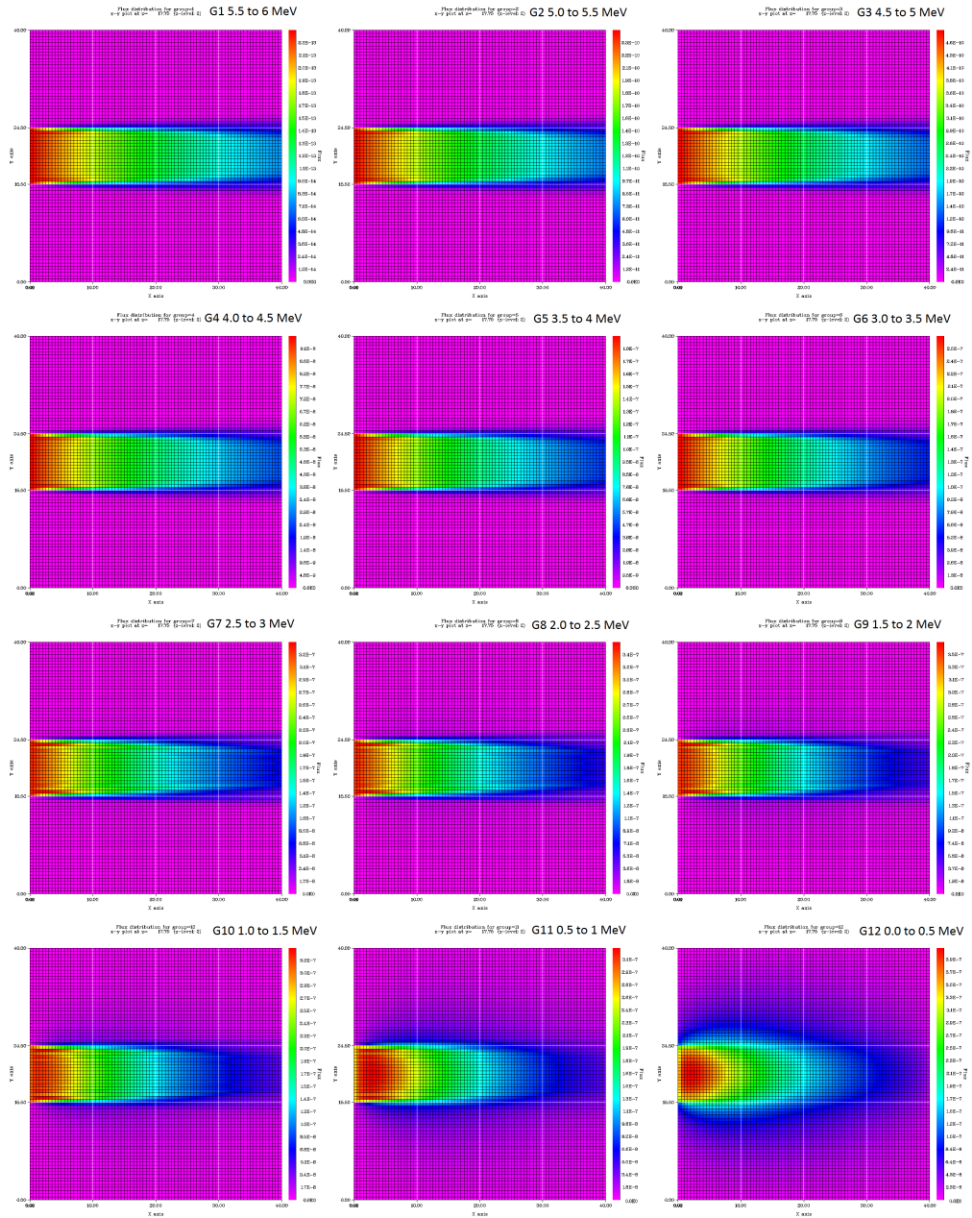
Figure 25. PENTRAN flux distribution using 0.5 cm mesh with S_{40} quadrature.
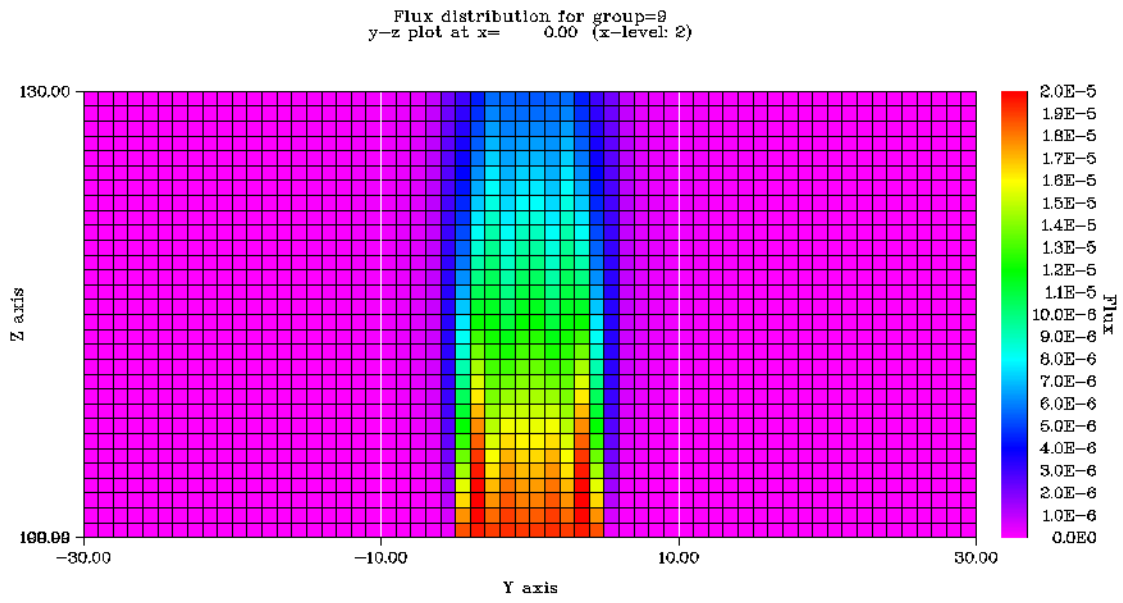
Figure 26. YZ plane view of flux in energy range 1.5 cm to 2 cm (photon flux) using 1 cm resolution.

4.2.2 Comparison of the EDK-S$_N$ Results to the Varian Golden Beam Data (GBD)

In order to compare EDK-S$_N$ to Varian GBD measurement data, a water phantom

problem is constructed with a 10 cm x 10 cm Varian TrueBeam impinging on a 30 cm x 30 cm x

30 cm water block. Figure 26 compares the PDD obtained with the EDK-S$_N$ method with that of

Varian GBD, and it shows an average error of 3.7%. This proves the EDK-S$_N$ method possesses

sufficient accuracy to match the midline dose using the phase space source term, discussed in

Section 4.2, and 12 energy group cross section modeled from CEPXS library. The quadrature

and Legendre moments for this model was S$_{62}$-P$_3$ using 0.5 cm x 0.5 cm x 0.5 cm fine mesh size.
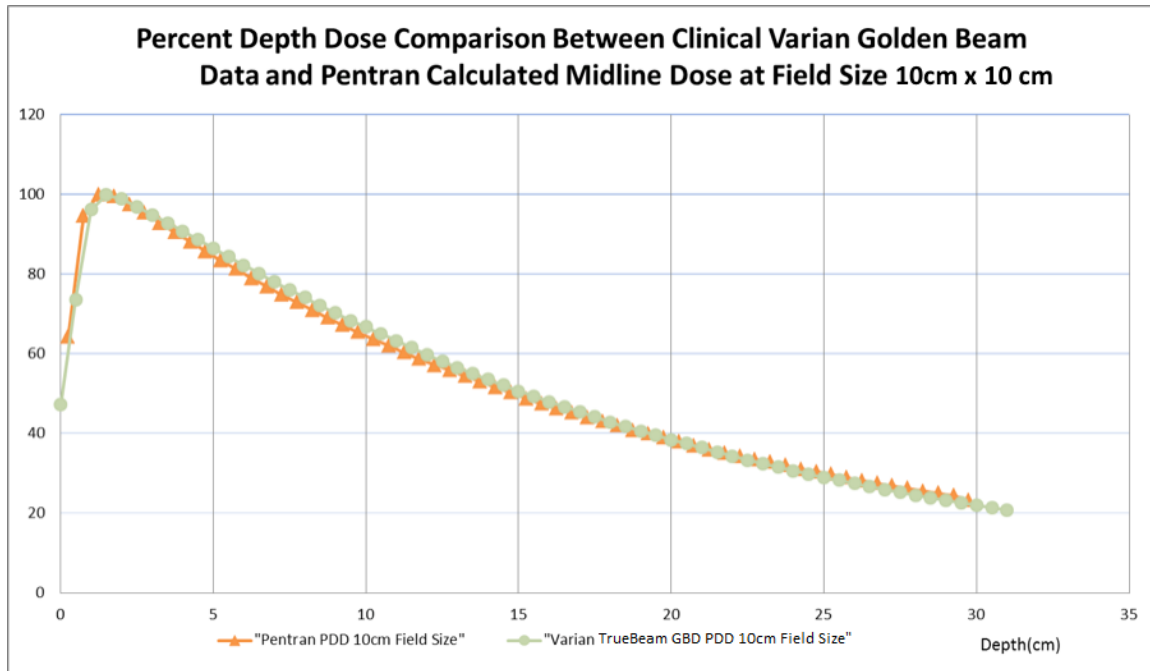
Figure 27. The comparison between the PDD obtained with the EDK-S$_N$ method and that of
Varian GBD. The average error is 3.7%.

CHAPTER 5

ADAPTING VARIAN PHASE SPACE TO MCNP PHASE SPACE AND

BENCHMARK WITH EDK-S$_N$ METHOD

This chapter discusses the importance of using Varian linear accelerator data, and provides a software framework that uses this data in MCNP and PENTRAN. The method of using Varian phase space data was favored versus the original proposal using publically available data sets. The adaptation of Varian phase space data to an MCNP phase space is performed in order to convert initial binary data to HDF5 binary(The HDF Group 1997-2015), a hierarchical data file format that is able to store large phase space data. The HDF5 binary file format is then converted to MCNP's surface source binary data structure. Figure 28 is a visualization of the phase space at the source plane using Varian TrueBeam data.
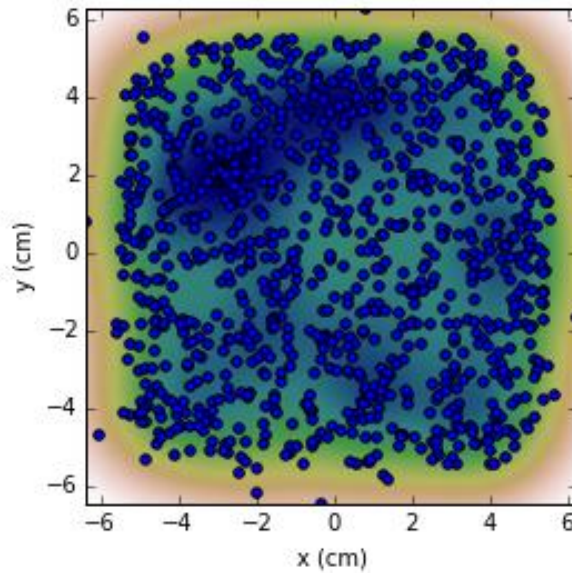
Figure 28. A subset of phase space 2D contour data of a Varian TrueBeam with 10cm x 10cm field size using PHSPMC in MCNP domain.

As previously researched, the International Atomic Energy Agency (IAEA) database included typical Varian and Elekta machine phase space information, and, depending on the specific machine, phase spaces that are usually located above the secondary jaws (Chetty, Curran et al. 2007, Fogliata, Vanetti et al. 2007). Instead of a single spatial representation, to improve the match to a clinical linear accelerator head source, a multiple radial ring model was applied to adapt an appropriate surface source in the discrete ordinates transport model. A typical Clinac head geometry is shown in Figure 29 and the head components are shown in Figure 30.
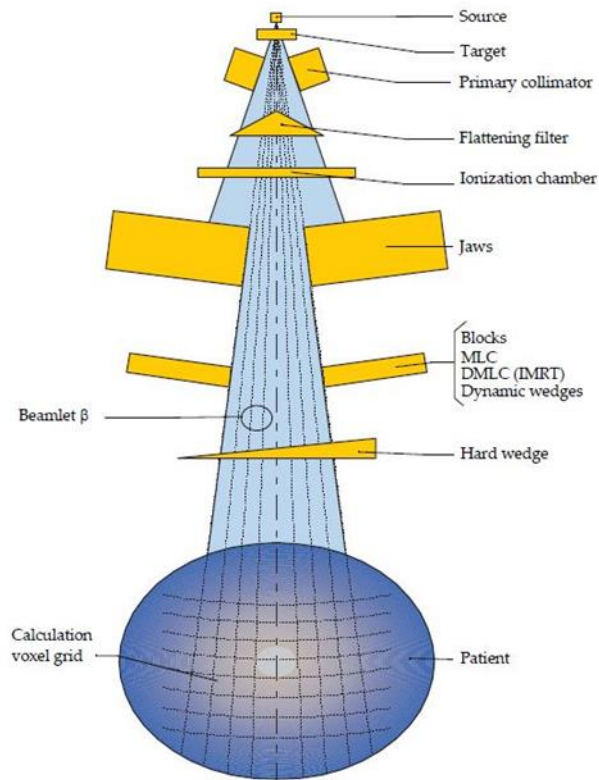
Figure 29. Illustration of Linac head modeling: full geometry with primary components – image reference: (Varian 2011).
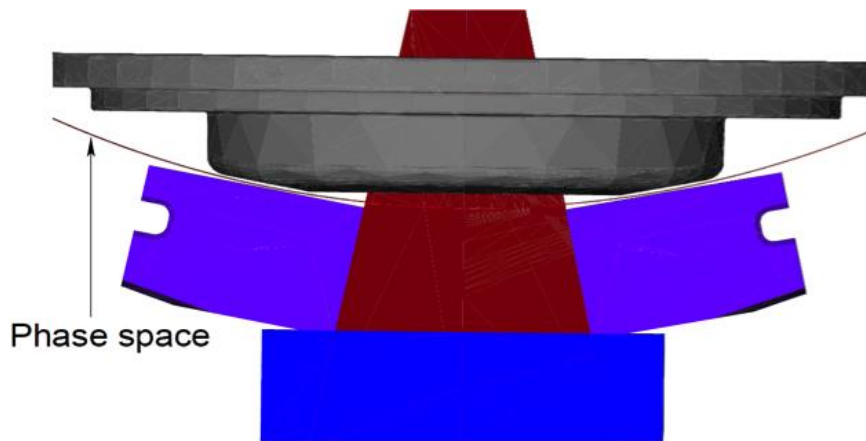
Figure 30. Geometry of the head components – image reference: (Constantin, Sawkey et al. 2011).

The phase space information provides the particle angle, space, and energy information from the Linear accelerator head model, but did not include the secondary jaws or any blocks, or MLC information. To include the secondary jaws and MLCs, the user has to define them specifically in the BEAM system to get new phase space information.

5.1 Converting Varian Phase Space Information to Surface Sources Suitable for MCNP

5.1.1 Defining Phase Space and Using Varian Data

A phase space, as defined in the medical physics community, is a set of particle track data. The data for each particle track include energy, particle type, direction of travel (2 variables in angle), and spatial position (3 variables for 3D). Therefore, at a minimum, 7 variables are needed to compose a single particle track on a scoring plane. A fully compliant phase space in practice applied to a Monte Carlo transport code would allow for sufficient fidelity.

Initial data provided by Varian phase space were provided using the standard formats recommended by IAEA (Capote, Jeraj et al. 2006). The reason for using the IAEA format is to provide a consistent phase space input data interface for codes such as GEANT4, EGSnrc, and PENELOPE, and other Monte Carlo codes. Varian Medical Systems, utilizes their full engineering diagram specifications of their hardware components to perform the most accurate model in GEANT4. A listing the recommended format for phase space is provided in Table 2.

Table 2: IAEA phase space format (Capote, Jeraj et al. 2006).

Variable	Meaning	Type	Size
X	X spatial position (cm)	Real	4
Y	Y spatial position (cm)	Real	4
Z	Z spatial position (cm)	Real	4
U	Direction cosine along X	Real	4
V	Direction cosine along Y	Real	4
E	Energy of particle in MeV	Real	4
Statistical_Weight	Weight of particle	Real	4
Particle_Type	Particle type	Integer	2
Sign_of_W	The sign of direction cosine W	Logical	1
Is_New_History	True/False if particle is new	Logical	1
Float_Extra	Extra float values (optional)	Real	n*(Real) n>=0
Integer_Extra	Extra integer values (optional)	Integer	n*(Integer) n>=0

Varian supplied TrueBeam phase space data, and were originally generated using the GEANT4 code. These data with the IAEA phase space format (Constantin, Perl et al. 2011) match the Golden Beam Data to within 1% for seven different photon beams (Constantin, Sawkey et al. 2013). Because of the high degree of accuracy, it is vitally important to make full use of phase space information provided by Varian.

One other benefit of the IAEA phase space format, is the compactness of the specification, as the files can be provided in a binary format suited for stream file I/O. Unfortunately, the concept of standardizing phase space particle track data was not a part of the MCNP development, as the code was originally developed based on the needs for nuclear physics and nuclear engineering applications. In order to write a particle track in MCNP, a tracklist (which is the same as a phase space) comprising 11 records shown in Table 3 is used in

the data/payload portion of the MCNP binary file. The format conversion process is discussed in the next section.

Table 3: MCNP tracklist format written by PHSPMC framework.

Variable	Meaning
Record	Number of 8-byte records in track (usually 11)
NPS	Index value for history
Bit Array	Particle type and has sign of W direction cosine
Weight	Particle weight
Energy	Energy in MeV
Time	Time value (not used for static/non-transient source)
X	X spatial position (cm)
Y	Y spatial position (cm)
Z	Z spatial position (cm)
U	Direction cosine along X
V	Direction cosine along Y
Surface	Assigned surface value (specific to MCNP)

5.1.2 Converting and Verifying Software Framework

Phase space data conversion to MCNP tracklist format is outlined in the following software framework, termed "PHSPMC" (Phase space to Monte Carlo for MCNP):

1. A Matlab script identifies individual phase space components, and converts the IAEA format phase space to the HDF5 (The HDF Group 1997-2015) file format.

2. The HDF5 file is read using Python and h5py (Collette 2013) library.

3. A Fortran binary file containing the surface source is written by using a template input deck with a surrogate surface source, similar to the MCNP input that will actually be run with the true phase space. This is achieved using the Python PyNE API (Scopatz, Romano et al. 2012).

4. The MCNP SSW (surface source write) binary file is written for use as a SSR (surface source read) in the active input.

In order to accommodate MCNP, the ability to write a suitable phase space was identified by writing surface sources to the SSR/SSW cards. This data was written using the specific Fortran format as was originally designed for the SSR/SSW option in MCNP. Of particular difficulty is the ability to write a binary surface source header, which was not well documented, as the surface source subroutines were not accessible for outside development, though it is available in the source code. To remedy the documentation issues, the PyNE (Python for Nuclear Engineering) API was used, as there was an ability to write phase space information from existing problems and properly form headers and payload/data from external phase space data. The phase space data conversion was accomplished by using a template MCNP input file with a surrogate source, which is nearly identical to the input file that is to be run using the Varian phase space. The reason that a template file is required is that MCNP writes header information that was not well documented – it was simpler to use MCNP directly to write a header using an existing problem, than identifying/aliasing a true original header from scratch. The PyNE API tool, which can be used with Python scripting, and in particular the API's MCNP

class is able to parse working problem outputs, making it easier to decode surface source headers.

Matlab was used as a primary tool for reading of binary data. In the course of this thesis investigation, the tool allowed for the automatic saving of 'workspace' data to HDF5 with Matlab 7.3+ and the higher versions (Mathworks 2015). This in turn allows a workspace in the Matlab GUI to be saved in the HDF5 h5 file format. The H5 file format is independent of the operating system, allowing for cross-platform work across Windows, Linux, and Mac OS platforms. As such, a user does not need to worry if the file is in 'Little-Endian' or 'Big-Endian' format.

In order to work with HDF5 in Python, h5py (developed by Collette) was used to interact with the data inside of Python script. The 'h5py' library was primarily intended to work with astronomic and space physics data comprising millions of data points (Collette 2013) but was always designed to allow for generic interfacing with HDF5. The HDF5 data format is generically suited for multidisciplinary science and engineering applications. One significant feature is the partial file I/O capabilities. This feature saves time and allows one to work with a file of gigabyte to terabyte size and access parts of file I/O data. Without this convenience, the files had to be read in before processing.

5.1.3 Validation of Framework with the Water Phantom Problem

To validate the data conversion framework, a MCNP calculation was performed with the phase space as the primary source term directed towards a 30 cm x 30 cm x 30 cm water phantom. The specific distances at 100.5 cm, 101.5 cm, 102 cm, 105 cm, 110 cm, 115 cm, 120 cm, 125 cm, and 130 cm from the source were tallied to generate PDD in the water phantom. These distances were chosen to align with the Varian GBD.

The computation times to generate PDD and radial dose profile (RDP) were on the order of days, but they can be reduced to several hours if it runs in parallel. Table 4 provides a listing

of computational wall clock times (wall time is measured by stopwatch– instead of user CPU time, time spent in non-kernel processes, which is less than or equal to wall time). Serial wall times are provided, as some of the parallel computations used a varying number of parallel processors, typically from 64 to 256 processors. Furthermore, providing the serial wall time is an appropriate indicator of the need for high performance computers, as model-based TPS calculations are limited to a few workstations that need to fit within the linear accelerator console area. Electron-photon collisions are roughly 1 million per single initial photon history. Furthermore, specific dose tallies are cast for each problem to simplify administration of data collection; with EDK-S_N the entire photon flux data is available, therefore, all dose data is available within a single computation. In real wall-time, computations in parallel are predominantly decided in phase space decomposition: for the PENTRAN water phantom problem, there are16 energy groups, 75 coarse meshes with 90,000 fine meshes, and a decomposition of 24 processors: 8 in angle, 1 in group, and 3 in space (with 8x1x3=24) . Regardless of how the problem is decomposed, EDK-S_N can obtain more accurate global results relative to Monte Carlo. In using Monte Carlo MCNP, specific tallies must be requested prior to the calculation start. Also interesting, is the lack of statistical confidence in out-of-field dose for Monte Carlo, despite the massive number of histories run; this is clearly another benefit for EDK-S_N, which is more consistent in driving flux and dose calculations within convergence parameters, which is fully expected as 3D SN transport fully solves for photon fluence to convergence within a user-specified inner tolerance (typically 1E-4) and folded with the dose projection.

Table 4: Computational wall time effort (* = average of fine mesh tallies) for dose.

Problem Type	Histories	Code	Average* Relative Error (%)	Serial Wall Time (minutes)
RDP	2.5 million	MCNP	4.477	8190
RDP	12.5 million	MCNP	2.792	40950
RDP	25 million	MCNP	1.134	81900
PDD	2.5 million	MCNP	1.023	7900
PDD	6.1 million	MCNP	0.1	39600
PDD	25 million	MCNP	<0.1	79000
RDP & PDD	N/A	EDK-S_N	0.5 *	4140

* Inner convergence tolerance = 1E-4 and Monte Carlo kernels were generated to be accurate to 0.5% relative error.

A series of graphs are now presented to demonstrate the accuracy of the successful conversion of the Varian phase space data for use in MCNP. Figure 31 shows the comparison of PDD obtained with MCNP with the Varian GBD, and Figure 32 provides the percent differences between the two data sets shown in Figure 30. Both Figure 33 and Figure 34 provide a set of RDP graphs and percent difference between GBD and MCNP results. Overall, matchups between GBD and MCNP are physically appropriate. In particular, both PDD and RDP comparisons are accurate, with errors generally below 2%. As a comparison, the error with EDK-S_N was previously shown to be less than 3.7% in Figure 27.

To obtain sufficient resolution in PDD and RDP, *F8 tallies were obtained using 10 or 20 times the original phase space by performing modified phase space concatenation, which is discussed in Section 5.1.4 Extending/Repeating Phase Space Information and Recommendations. Figure 35 and Figure 36 show, respectively, the PDD and associated relative errors. Figure 37

and Figure 38, respectively, show the RDP at chosen depths and the associated relative errors. For the PDD case, the basis phase space is shown where statistical noise is present in Monte Carlo, which is not present in EDK-S_N. The EDK-S_N inner tolerances are set to 1E-4.
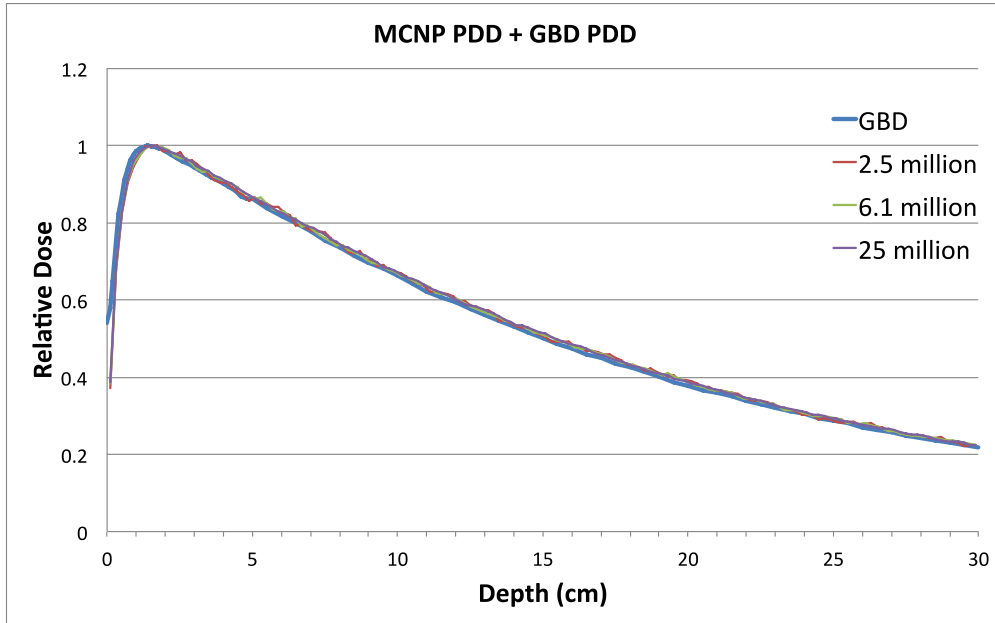
Figure 31. Comparison of PDD obtained with MCNP and the Varian GBD.
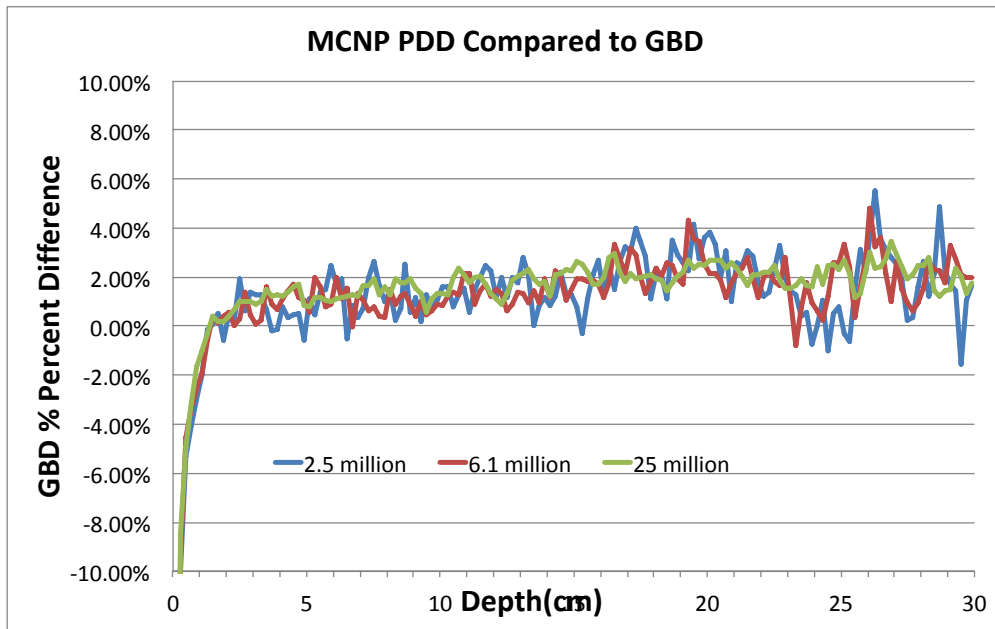
Figure 32. The percent differences between the PDD obtained with MCNP and the Varian GBD.
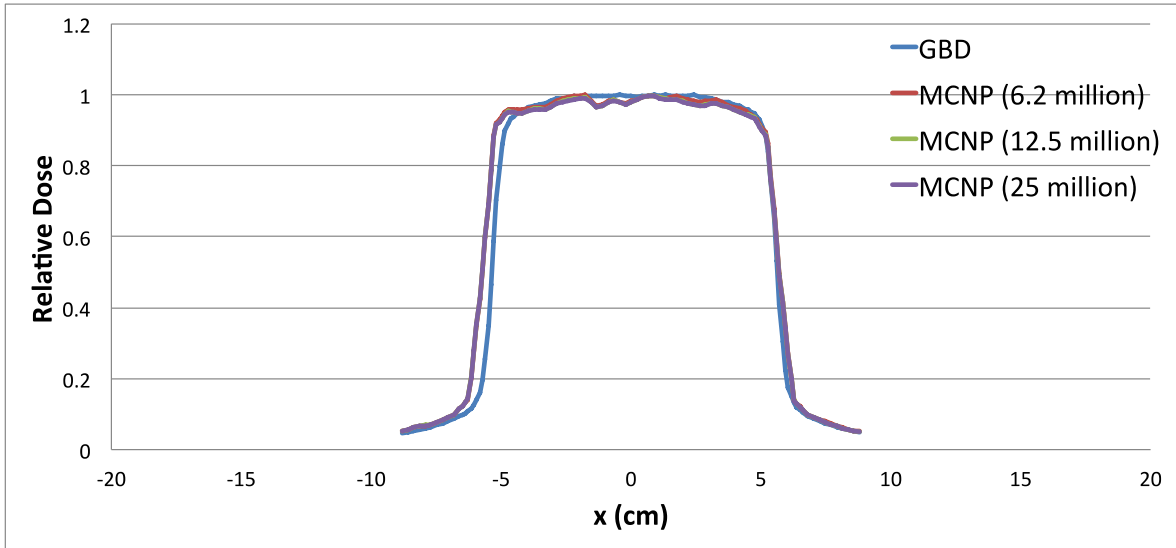
Figure 33. Comparison of RDP obtained with MCNP and the GBD.
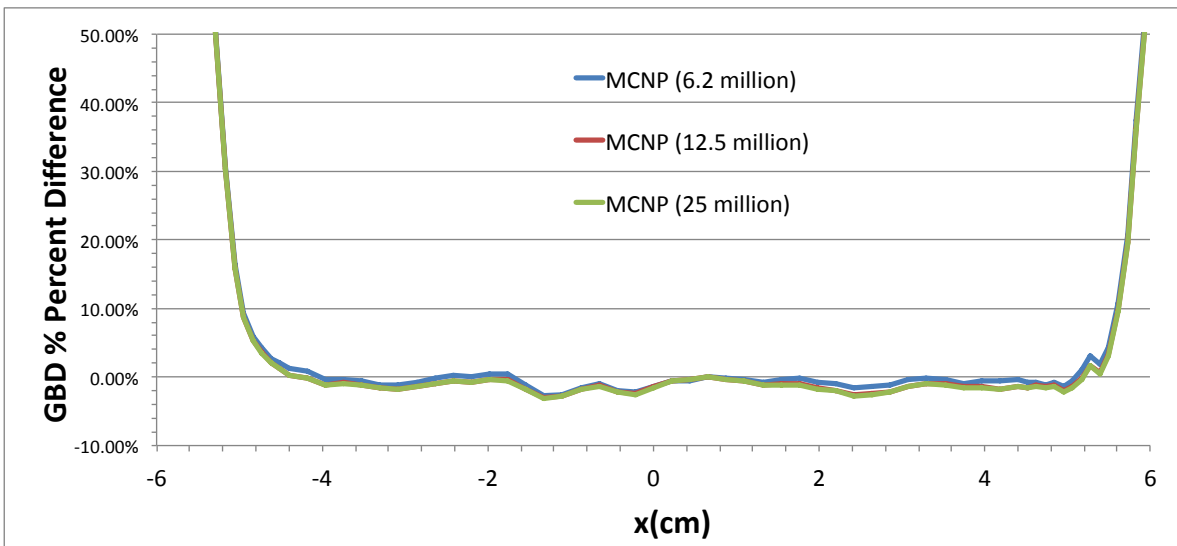
Figure 34. The percent differences between the RDP obtained with MCNP and the Varian GBD.
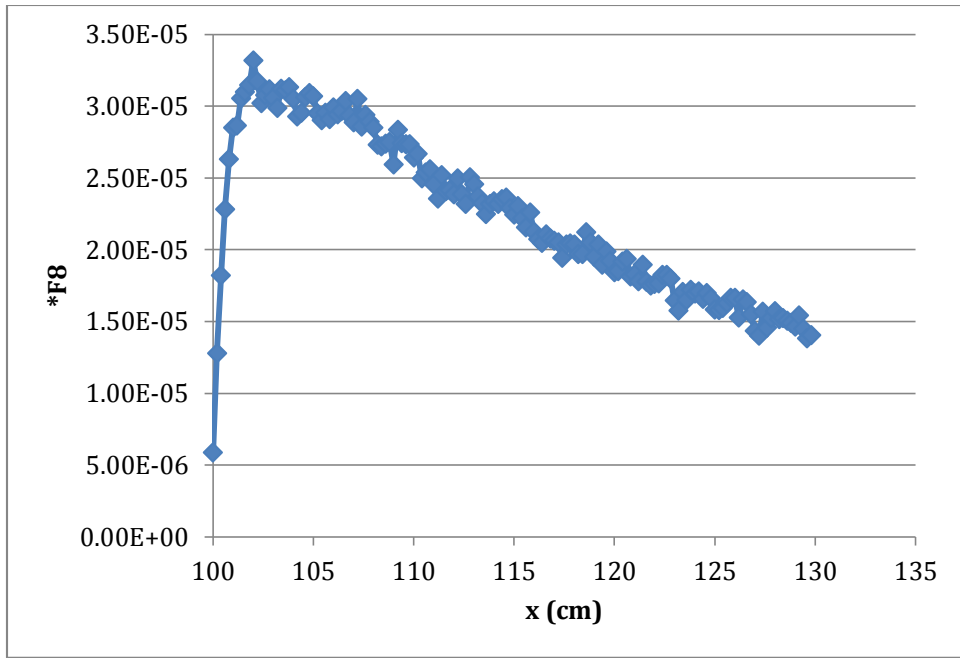
Figure 35. The PDD obtained with the *F8 tallies with 2.5 million photon histories. The statistical fluctuation is clearly shown.
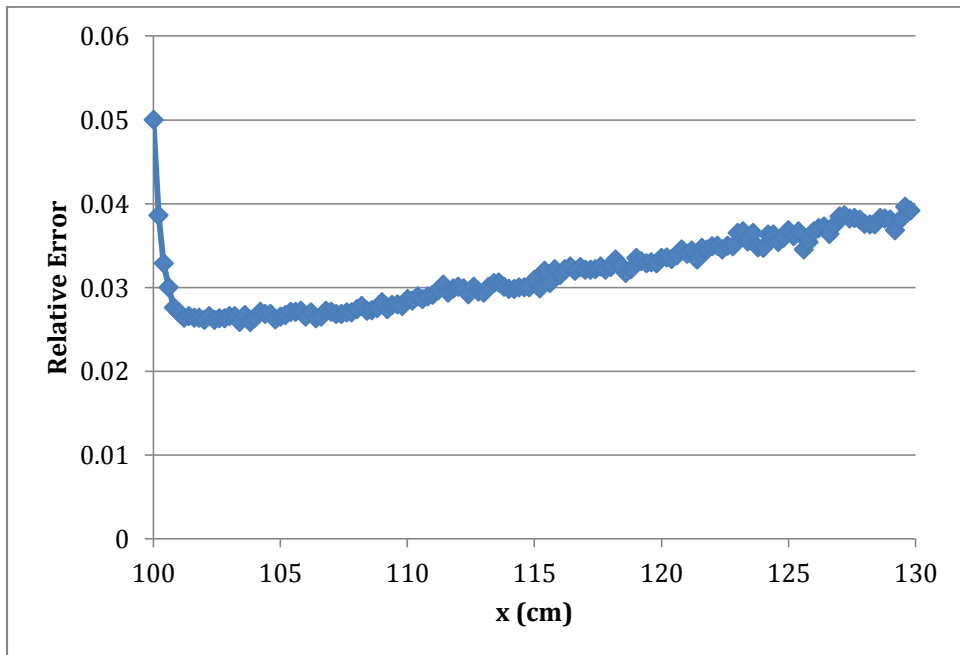
Figure 36. The relative errors associated with the PDD obtained with the *F8 tallies with 2.5 million photon histories.
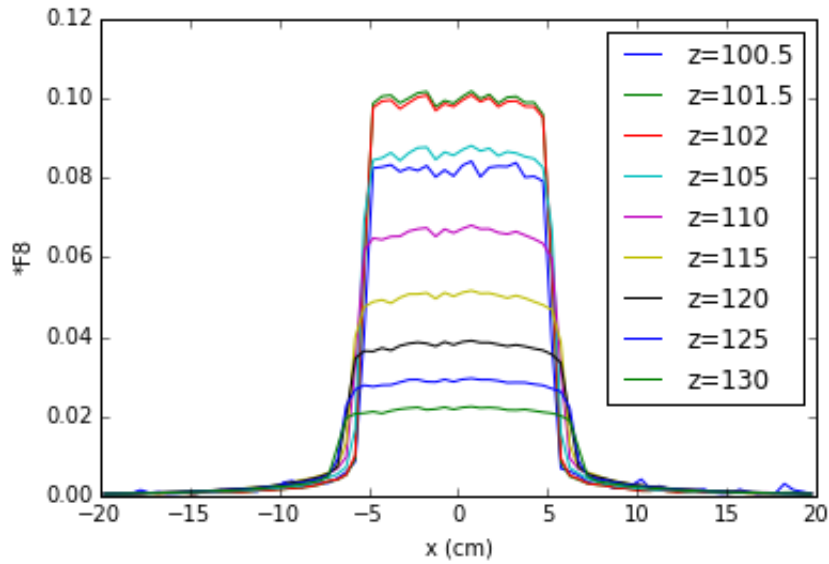
Figure 37. The RPD obtained with the *F8 tallies along a water phantom for various depths (with the phantom front face at z=100 cm) with 50 million photon histories.
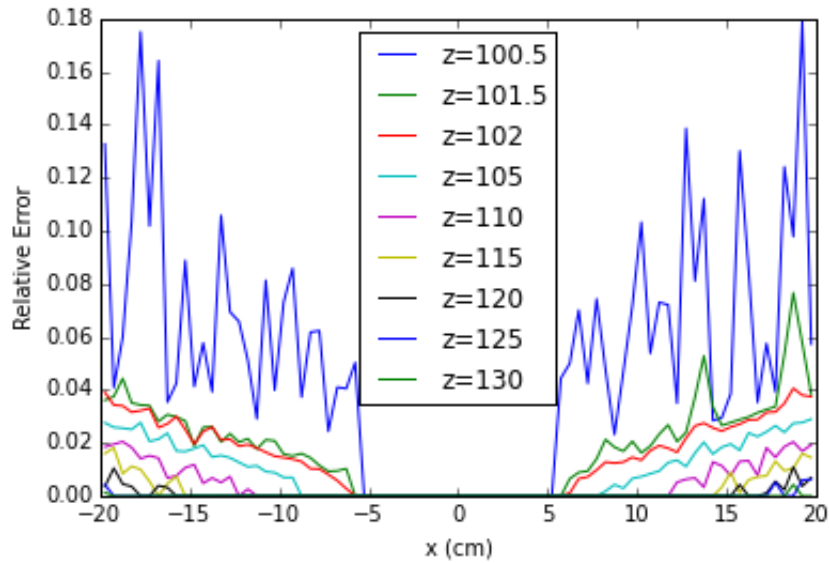
Figure 38. The relative errors associated with the RPD obtained with the *F8 tallies. along a water phantom for various depths (with the phantom front face at z=100 cm) with initial histories of 50 million particles.

5.1.4 Extending/Repeating Phase Space Information and Recommendations

Varian provided phase space data in the size of 2.5 million photons, which is often not enough for MCNP to produce statistically acceptable results. In order to significantly increase the photon histories, the phase space data can be multiplied. However, this requires header adjoined to multiple tracklists. The header itself must be modified in order to increase the total number of tracks. Hence, using the PyNE API along with basic Linux utilities is needed to grow the phase spaces as necessary. Some of the larger file-sets were in excess of 1 TB; hence, further growth became impractical working on a high performance computing (HPC) cluster limited to a few TBs. The procedure for modifying the MCNP surface source is shown in Table 5.

Table 5: Modifying MCNP surface source.

Format	Surface Source Format		
Standard	Header		Tracklist
Concatenated	Modified Header	Tracklist	Tracklist Copy (times N)

5.2 Future Work and Recommendations for Phase Space Applications with MCNP

This chapter provides a conversion of GEANT-4 phase space data in IAEA format to MCNP's data format. Without this work, it would not be possible to generate comparisons of EDK-S_N to MCNP for calculating organ doses using Varian phase space data.

The current software framework is sufficient to convert the Varian phase space data to MCNP surface source input. There are several recommendations for future work in this regard. The first recommendation is to consolidate the software package into a single Python script. The second recommendation is to improve the scalable parallel file I/O using HDF5. Since wall clock phase space file format processing takes 15 minutes to 2 hours, adding parallelization to

file I/O would reduce the time. The third recommendation is to improve the surface source subroutines in the Fortran/C components in MCNP. This requires some collaboration with the Los Alamos National Laboratory (LANL) MCNP development team. One noted weakness of the surface source phase space is the inability to perform a 'continue' run. This can be done with a defined SDEF forward source term in the input deck. The current strategy is to concatenate multiple tracklists. This strategy was conveyed in Table 5 in the previous section. The fourth recommendation is to coalesce the PHSPMC framework underneath a single language. The logical choice is to reduce all the steps of the framework to Python scripting, as it is necessitated from using PyNE. The performance of the phase space modification could also be improved by writing in compiled C language.

In summarizing the computational results, the MCNP results indicate that the statistical errors associated with the Monte Carlo Calculation for out-of-field doses could be up to 20%. The deterministic EDK-S_N method eliminates the increasing statistical errors for out of field dose, as indicated in the previous chapter. The final set of dose calculations using both the MCNP and EDK-S_N for whole-body organ doses will be demonstrated in the next chapter.

CHAPTER 6

ORGAN DOSE CALCULATIONS FOR A 15-YEAR OLD MALE PHANTOM: COMPARISON BETWEEN MCNP AND EDK-S$_N$

The University of Florida ALRADS group provided computational phantoms with detailed organ identification (Bolch, Lee et al. 2010) based on the real CT patient data. The ALRADS phantom data were provided in 0.2cm x 0.2 cm x 0.2 cm resolution. In this chapter, a 15-year old male phantom data (302 mm x 139 mm x 836 mm) was used by both EDK-S$_N$ and the MCNP, and the results are compared. The patient phantom global boundaries span x from 0 to 60 cm, y from 0 to 27 cm, and z from 0 to 167 cm.

6.1 Implementing the Phantom to MCNP and PENTRAN

The phantom data was first processed by the GHOST-3D code (Ghita, Al-Basheer, and Huang) to obtain the suitable voxel size data. The resolutions for this study were updated to match those used in the EDK kernel, which was improved from 1 cm to 0.5 cm. The increase in resolution by a factor of 2 required an 8-fold increase in computer memory for a 3D phantom calculation. In order to permit the problem to fit on Georgia Tech's PACE HPC platform, a truncated chest model was used such that the overall mesh number would only increase by a factor 2 compared to the original 1 cm resolution model. The global boundaries for the truncated phantom span x from 0 to 40 cm, y from 0 to 27 cm, and z from 0 cm to 59.5 cm. Individual organ material voxels were simplified to four principal materials: bone, air, tissue, and water. This approach reduced the runtime memory storage of cross sections, and also simplified EDK-S$_N$ in application of heterogeneous correction.

Figure 39 is an iso-surface view of the full patient at 1.0, 0.5, and 0.2 cm resolutions. Figure 40 is a sagittal view of the 15 year-old male phantom with selected organ identification (Lee, Lodwick et al. 2008). Figure 41 is a sagittal view of the four material phantom model with 1.0 cm and 0.5 cm resolution as a result of downsampling. Figure 42 is an alternative coronal view.
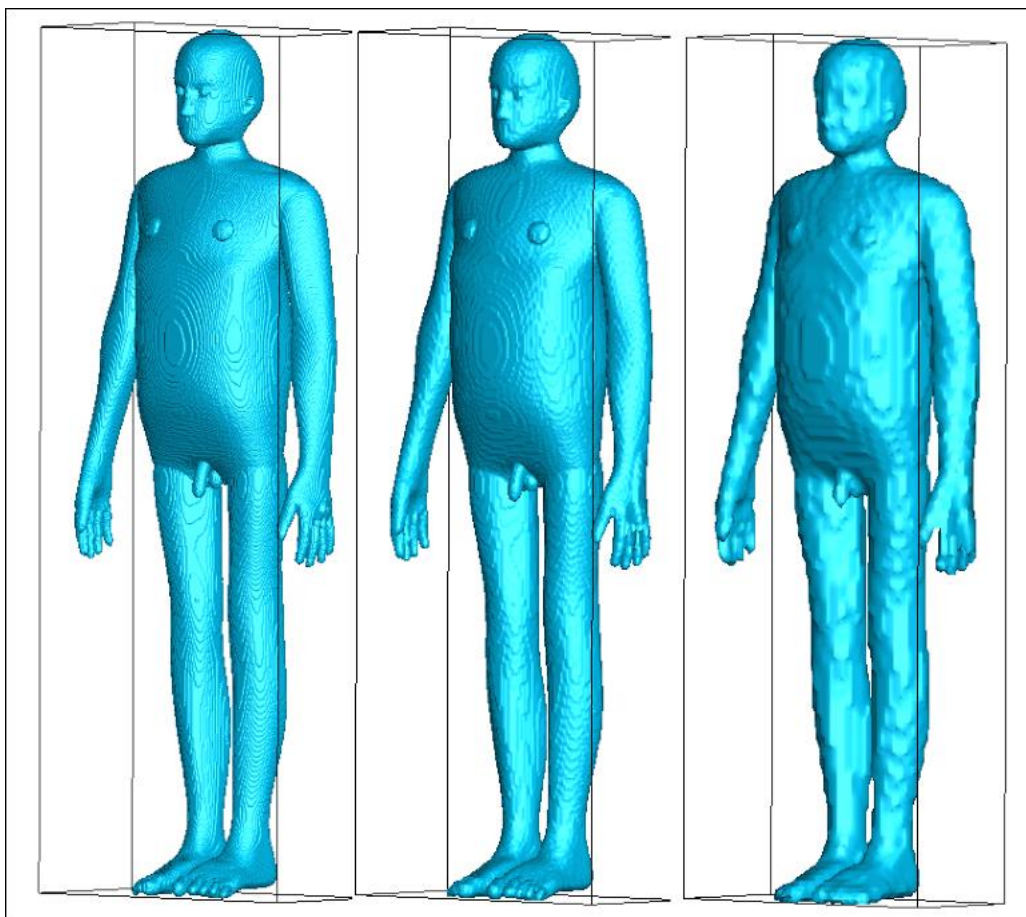
Figure 39. The 15-Year Old ALRADS patient phantom with 2 mm, 5 mm, and 1 cm voxel resolutions (iso-surface shown).
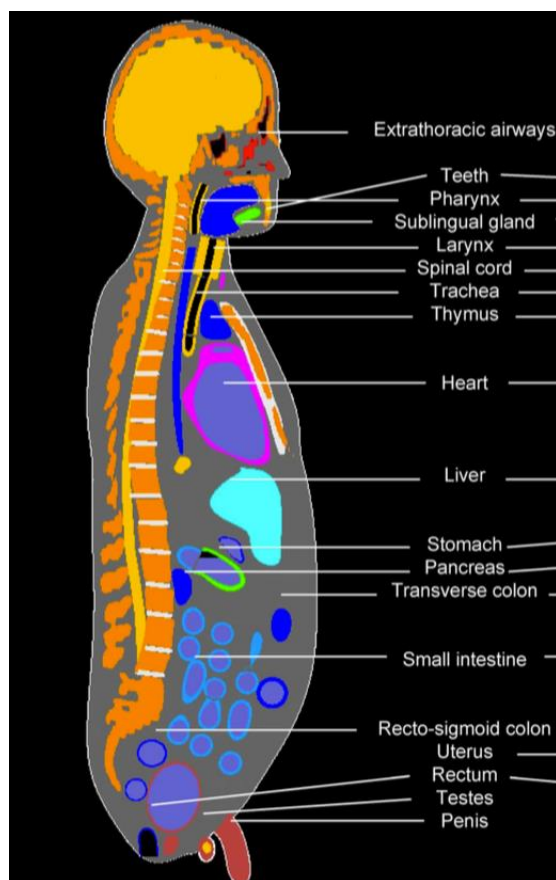
Figure 40. The 15-Year Old Male ALRADS phantom sagittal view with organ identification (Lee, Lodwick et al. 2008)
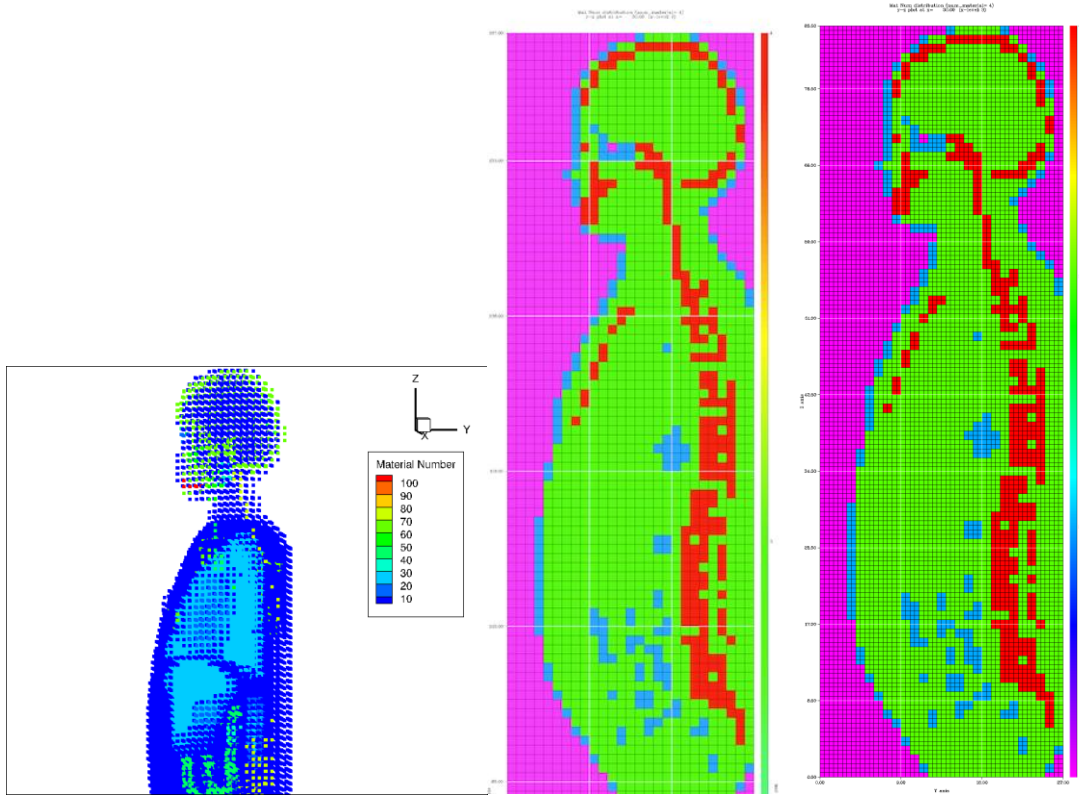
Figure 41. (b) A partial sagittal view of the full patient phantom modeled in MCNP, and (b) A sagittal view of the 15-Year Old NURBS/ALRADS phantom modeled in PENTRAN with two voxel sizes, 1 cm and 0.5 cm modeled in PENTRAN.
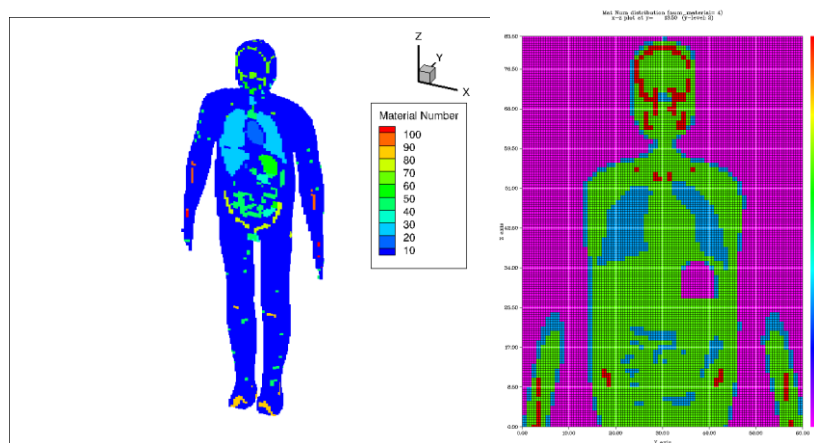
Figure 42. (a) A coronal view of the full patient phantom modeled in MCNP, and (b) A coronal (cross section) view of the patient phantom with four material cross sections modeled in PENTRAN.

The full phantom model spanned x from 0 cm to 60 cm, y from 0 cm to 27 cm, and z from 0 cm to 167 cm with a volume of 270540 cm^3 , occupying 2.1 million fine meshes with 0.5 cm mesh resolution. The truncated chest model reduced the dimensions (in x, y, z) to 40 cm, 27 cm, and 59.5 cm, with volume 64,260 cm^3 occupying 514,080 fine meshes with 0.5 cm mesh resolution. The location of the 10 cm x 10 cm field size source is shown in Figure 43, which spans x in width from 15 cm to 25 cm, y equal to 0 cm, and z from 37.5 cm to 47.5 cm. The final truncated chest phantom model and flux in the lowest energy group in log-scale are shown in Figure 44.

The source model applied the ring-based technique presented in the last chapter, as part of the results of the PHSPMC framework. The resulting calculation used S_{50} quadrature and P_1 Legendre moments in the (12 group) multi-group cross sections. The full model is highly scalable given more processors and memory. The calculation was performed using 672 MPI tasks, with 5.5 GB per processor using 12 nodes of 56 CPUs, and was completed in a wall time of 139 minutes. It is important to consider the computational time, as it needs to be fast enough to satisfy the daily clinical workflows.

The EDK-S_N calculation of dose mapping was performed upon successful convergence of the PENTRAN calculation of both scalar flux and magnitudes of current. The MCNP calculation was performed with the phase space derived from PHSPMC framework. Increasing phase space histories were considered in order to reduce the statistical errors due to fine mesh tallies, as shown in Table 7. Because different numbers of processors were used for various computations, equivalent single node (64 CPU) parallel computation wall times are estimated from the MCNP provided computer times to allow for appropriate comparisons. The EDK-S_N calculation is efficient in providing whole body dose everywhere in the phantom without

69

statistical error within 2 hours of wall clock time; however, in comparison, with Monte Carlo, to achieve less than 1% error in dose calculation takes 15.31 hours on 64 CPUs.

To simplify comparison, only organs with sufficiently small relative errors (< 1%) and the organs in the chest region were considered. The Varian TrueBeam phase space source is verified by using the mesh tally option for flux to visually confirm proper source term placement; the natural logarithm of relative flux is shown in Figure 45 and the corresponding relative error is shown in Figure 46 using the MCNP case with 4800. Normalized organ doses (cGy) are obtained from cell *F8 (MeV) tallies in MCNP, multiplying 1.6 E-8 Joules per MeV, then dividing by cell mass to obtain dose in cGy. At 1.5 cm water depth, the source delivered is normalized to 100 cGy using a 10 x 10 cm field. Similarly, EDK-S_N results are accumulation of doses as a function of fine mesh for the specific organs shown in Table 6. The organ doses obtained with MCNP and EDK-S_N agree with each other to within a range of -6% to 13%.

The EDK Monte Carlo kernels for the lung are scaled for heterogeneity corrections according to the lung voxel electron density, of 0.26 to 1 relative to water electron density (Khan and Gibbons 2014), as applied similarly with the Eclipse AAA lateral scattering kernel correction method (Varian 2011). The primary photons and inter-voxel scattering fluence for different voxels in the phantom are directly calculated by the PENTRAN deterministic method, corresponding to the different material cross section information for each voxel. Final absorbed doses are also obtained by dividing by the local material density in g/cc for each voxel in EDK-S_N method.
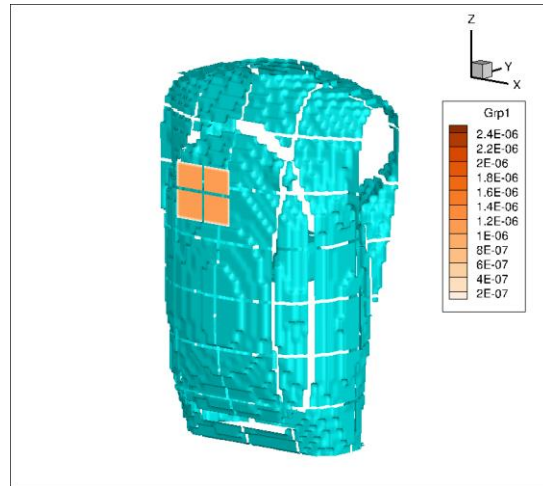
Figure 43. An iso-surface of the truncated chest phantom model with source on xz plane, which spans x in width from 15 cm to 25 cm, y = 0 cm, and z in height from 37.5 cm to 47.5 cm in the model.
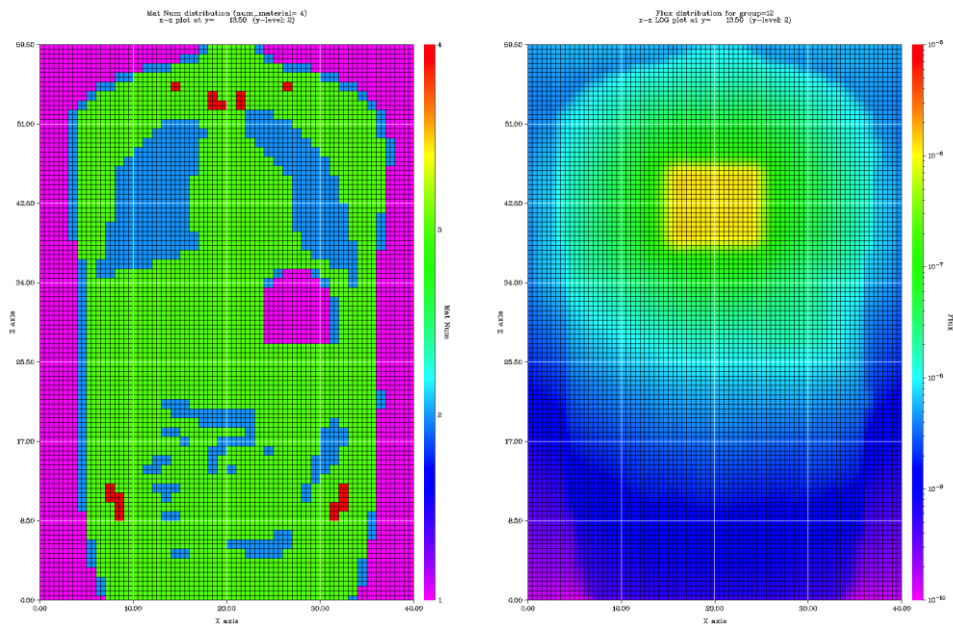
Figure 44. PENTRAN S_N model and flux calculation: (a) A cross-sectional view of the truncated chest phantom and (b) a plot of relative photon flux in log scale of the lowest energy range.
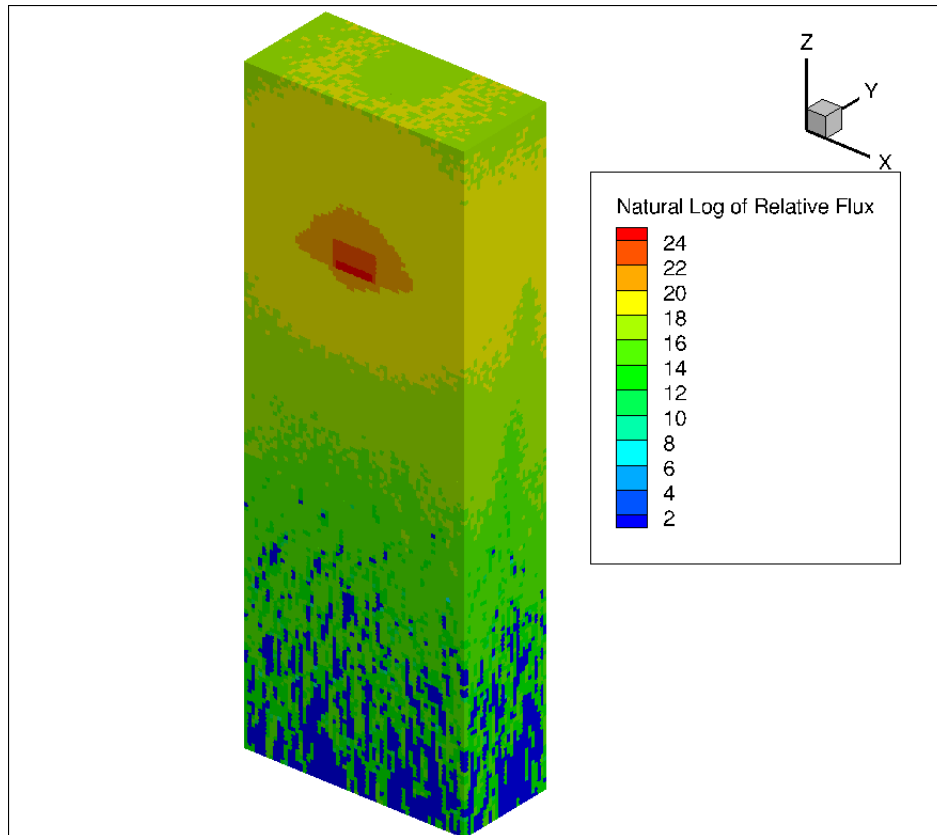
Figure 45. A confirmation of the total (sum of all energies) phase space source term using total F4 mesh tally option in MCNP (4800 computer minutes).
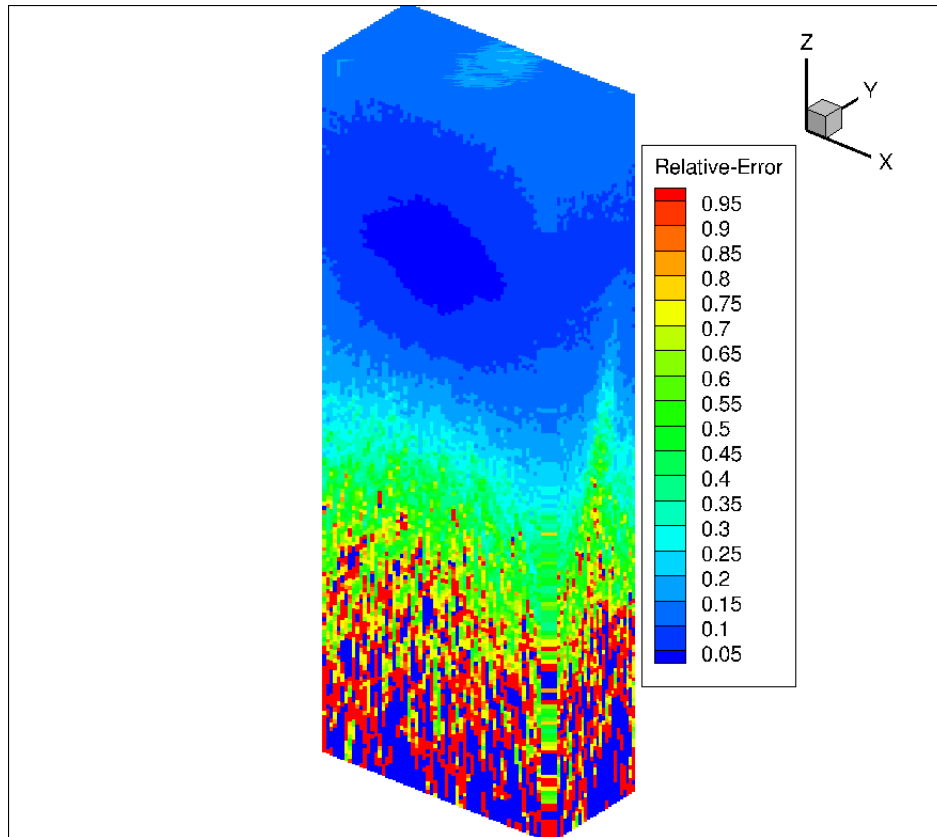
Figure 46. A corresponding view of relative error of the F4 mesh tally with a selected MCNP calculation (4800 computer minutes) with relative error increasing as a function of distance from the phase space source.

Table 6: Comparison of relative organ absorbed doses (*F8 = MeV) obtained with MCNP and EDK-S_N.

Organ / CM Position[1]	Density (g/cc)	Volume[2] (cc)	Normalized Mean Organ Dose (cGy)[+]	*F8 Rel. Error (%)	EDK-S_N Dose (cGy)	% Difference (MC-EDK)/ MC
Source (30, 0, 127.5)	-		1.000E+02	-	-	-
Heart (31.78, 12.56, 126.2)	1.05	609	1.614E+01	~0%	1.576E+01	2.34
Thymus (29.90, 14.81, 135.7)	1.03	32	1.538E+01	~0%	1.501E+01	2.38
Lung(R) (23.32, 16.75, 126.8)	0.24	2043	5.188E+00	~0%	5.392E+00	-3.94
Lung(L) (37.58, 17.31, 127.2)	0.24	1715	4.713E+00	~0%	4.991E+00	-5.92
Liver (24.85, 12.15, 114.2)	1.05	1230	2.644E-01	~0%	2.504E-01	5.28
Gall Bladder Content (28.03, 13.08, 111.6)	1.03	45	2.581E-01	0.58%	2.250E-01	12.83
Pancreas (34.30, 16.83, 108.4)	1.04	108	1.954E-01	~0%	1.730E-01	11.46
Stomach Content (35.25, 12.39, 109.1)	1.02	208	1.954E-01	~0%	1.715E-01	12.27
Small Intestine Wall (29.91, 14.25, 98.64)	1.03	770	1.473E-01	0.84%	1.317E-01	10.53

[1] Center of Mass Position in the Full Phantom, MC Computer Time = 66331, Sn Toler. = 1E-4
[2] Some volume differences between original 15-year UF NURBS phantom result from downsampling.
[+] *F8 Tally in MeV converted to cGy

Table 7: Reduction of *F8 (based on 'SI wall' tally) relative error with increasing particle histories for MCNP calculation (wall time for PENTRAN calculation was 139 minutes).

Histories	Relative Error (%)	Improvement Factor	Computer Time (serial)	Equivalent Wall Time (hours) (on 64 CPUs) (parallel)
-	35.36	-	4857 minutes / 80 hours	1.25
2.5 million	4.09	8.64	15903 minutes / 265 hours	4.14
25 million	0.84	42.1	66331 minutes / 1105 hours	17.27
Deterministic EDK-SN	0.5*	NA	Parallel	2.3

* SN Inner Tolerance = 1E-4, $S_{50}P_1$

6.2 Discussion for the EDK-S$_N$ Method

It is important to conclude the status of the EDK-S$_N$ methodology, and recommendations for additional research. Identification of the EDK method limitations can provide insights on improving both EDK and similar methods. As it pertains to the EDK method, limitations related to use of the MCNP energy cutoff card are discussed.

Without the energy cutoff, the intergroup photon interactions are over-counted due to the primary photons contributions from other groups. The over-counting is unavoidable, as problem physics are duplicated with each subsequent source window. Hence, the total dose is overestimated, and this is progressively worse with increasing the number of source windows. This overestimation is shown in Figure 47.

With the energy cutoff, any photon particle generated below the source window, does not account for the subsequent secondary bremsstrahlung generated; this underestimates the total amount of photons due to secondary electron-induced bremsstrahlung photons; hence, the total dose is underestimated, as shown in Figure 48. In the application to EDK-S$_N$ for the thesis, a cutoff was applied not to double counting the intra-energy groups' photon scattering. Although the energy no-cutoff kernel will preserve the bremsstrahlung photons, however, at 6 MeV, this portion is only at less than 1% of the total electron deposited (Khan and Gibbons 2014). Therefore, final calculation used the cutoff card to stop particle transport below that energy group in MCNP.

Satisfactory results to meet the proper in-between model may be obtained by providing modifications to the energy cutoff card (in source code). One recommendation is to perform the EDK application within GEANT4, using the C++ API. The Monte Carlo tool is programmable to detail energy cutoff assumptions.

In summary, the accuracy falls between the two models, as simple averaging is not a problem-specific approach, with specific patients spanning wide ranges with age, size, and physiology.

There is another significant physics limitation, which is the assumption that EDK makes in aliasing the net current to project the cloud dose kernel; an even more accurate handling of the dose kernel could be calculated by applying detailed information directly from angular flux, which PENTRAN can provide. Use of the net current reduces the angular contribution, in such a way that the cloud dose kernel is biased to co-align with the beam, instead of accounting for multiple sub-component contributions along each discrete ordinate path. However, requiring angular flux detail in PENTRAN for each spatial fine mesh, is a significant storage hurdle; for example, S_{62} quadrature would require the storing of angular flux information across 3968 ordinates for a single fine mesh. Outside of the thesis scope, one improvement would be to embed the EDK calculation directly inside the PENTRAN source code to create a dedicated application, and avoid the angular flux overhead.

One other limitation is the beam divergence and modeling capabilities limited by discrete ordinates transport. Increasing the field area of the beam at a distance works to improve the source term model. Additional memory savings are needed - one improvement is to reduce the overhead in angular flux storage and pre-calculate contributions to the angular flux moments.
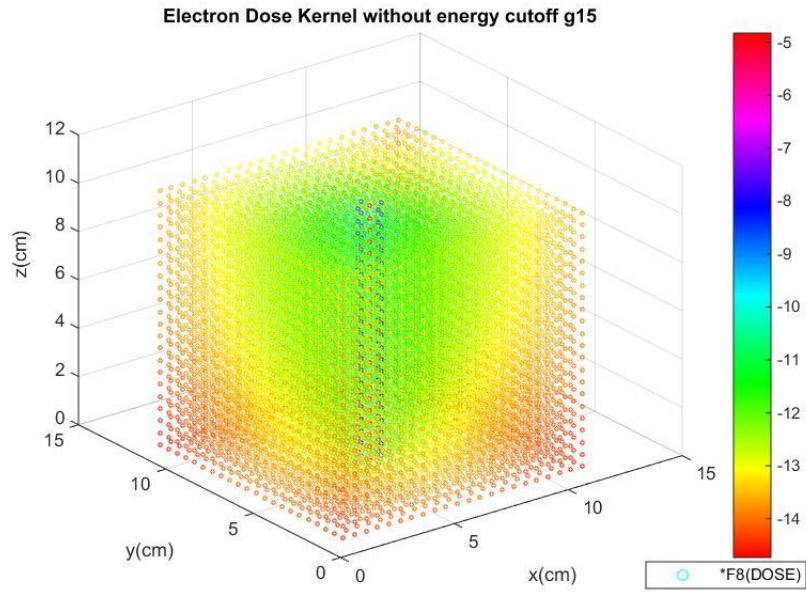
Figure 47. Electron dose kernel with no energy cutoff for energy range 0.5 to 1 MeV.
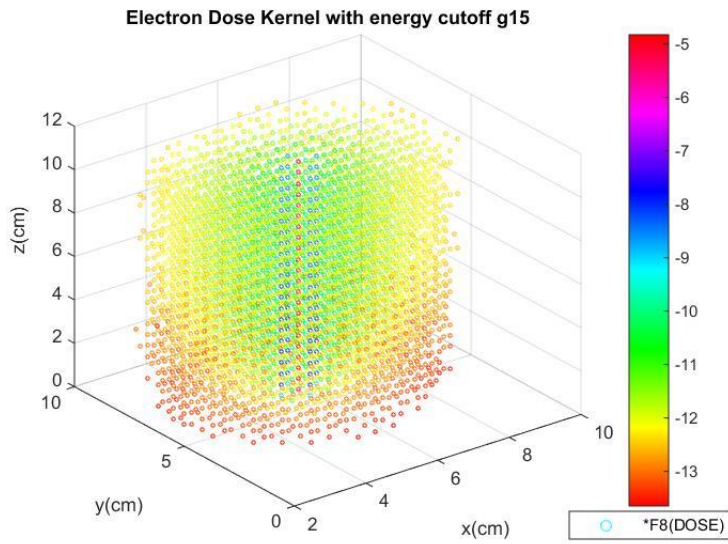
Figure 48. Electron dose kernel with energy cutoff for energy range 0.5 to 1 MeV.

6.3 Summary of Improvements to EDK-S_N Method

The thesis demonstrates several advancements of the EDK-S_N method:

1. An improvement to source term accuracy for deterministic photon transport calculation using PENTRAN.

2. An improvement of source modeling by constructing spatial PDFs converted from the clinical linear accelerator particle phase space data.

3. An improvement in rotation algorithm by using quaternion rotation.

4. An improvement in fine mesh grid from 1.0 cm to 0.5 cm.

5. A different heterogeneity correction method was used to obtain absorbed dose in lung organs.

The listed improvements are an evolution of the original EDK-S_N method (Al Basheer 2008) with a focus on modeling with accurate source terms that are representative of the linear accelerator beams, for both Monte Carlo and S_N transport calculations. The EDK-S_N method is effective in a water phantom problem compared to the measured clinical golden beam data. This is sufficient in proving the accuracy of the method as well as demonstrating the superiority in computational speed versus the Monte Carlo method. It has also been shown that the absorbed doses, in both water and real patient phantoms calculated with the improved EDK-S_N method, agree well with that obtained with the MCNP method.

CHAPTER 7

CONCLUSIONS

In conclusion, this thesis presented a new and fast dose calculation tool called EDK-S_N. The method effectively uses Monte Carlo electron dose kernels driven by linear photon deterministic transport. In addition, the thesis improves on EDK-S_N deterministic source term modeling and provides a software framework for converting Varian TrueBeam phase space data for use in MCNP. Also, the EDK-S_N method was effectively benchmarked using water phantom calculations to Varian golden beam data to within 3.7% difference. Finally, selected organ doses for a 15-year-old male phantom calculated by MCNP and EDK-S_N were compared and the results agree with each other to within -5 to 11%.

The EDK-S_N also demonstrates speedup compared to Monte Carlo with the use of parallel computational resources, taking 2 hours to perform an 3D whole body converged organ dose computation in a computational 15-year-old phantom, whereas the Monte Carlo computation takes 16 or more hours to achieve similar error goals.

APPENDIX A

APPLICATION OF DETERMINISTIC TRANSPORT METHOD IN

MEDICAL PHYSICS: GEORGIA TECH CLINICAL SHIELDING

TRANSPORT CALCULATION

The below work demonstrate multi-group cross section development with S_N computation for photon flux, to compute adjoint response for linear accelerator in medical physics shielding calculation. This work is to demonstrate the novel S_N application for medical physics application, and is adapted from the authored transaction (Huang, Manalo et al. 2012). This study is tangentially related to the thesis, by relation to its connection to the research Clinac at Georgia Tech. More importantly, this study motivated the initial 6MV and 18MV commissioning spectra study, which ultimately led the pathway for researching Varian-generated phase space data.
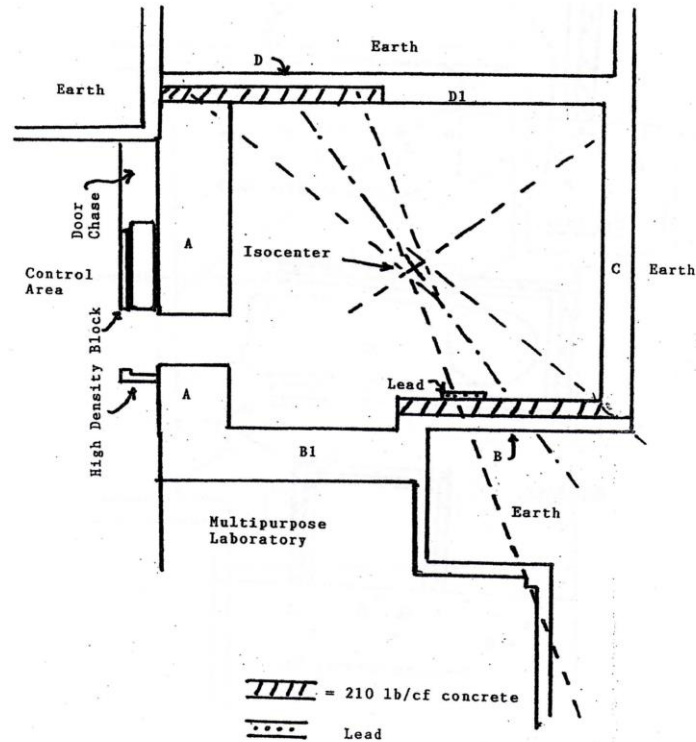
Figure 49. Georgia Tech Boggs building basement clinac vault shielding floor plan (McGinley 2011).

Regulatory shielding designs are conservatively over-designed and thus yield an increased concrete shielding cost. Again, the most important issue is to identify a computational framework to justify a reduction in shielding requirements, starting with a computational evaluation of detector fluxes in concrete shielding, by performing deterministic transport calculation and continuous and multi-group Monte Carlo transport codes.

Based on a single source spectrum representative of a Clinac 6 MV head adapted from the Varian treatment planning system, transport calculations were performed to estimate the photon flux after concrete shielding. Materials involved were a 10 cm concrete shield, and a 1 cm detector. The purpose of the study was to compare flux between Monte Carlo and deterministic (S_N) codes, with the objective of understanding differences in S_N multi-group flux behavior to Monte Carlo (continuous and multi-group). This research was intended to provide a

reduced multi-group structure for future S_N shielding transport calculations. As linear photon transport only calculates photon flux, dose calculations are only then determined via photon-electron dose conversion tables.

Practical dosimeters in use today at radiotherapy facilities are typically badge dosimeters, such as Al_2O_3 for optically stimulated luminescent dosimeters / thermoluminescent dosimeters (OSLD/TLD), and LiF (TLD). Energy responses for these materials are well characterized, for example, see Mobit's paper on energy response factors for LiF and Al_2O_3 (Mobit, Agyingi et al. 2006) and Scarboro's paper on applying cavity theory for determining energy response for Al_2O_3:C OSLs (Scarboro and Kry 2013). The use of LiF and Al_2O_3 dosimeters are commonly used in verification of patient entrance dose in radiotherapy and also for standard detector badges. Therefore, LiF and Al_2O_3 were selected as primary detector study materials.

A1.1 Description of Spectrum Source Term Used for Shielding Analysis

The Varian Clinac iX series operates with both high-energy photon beams and electron beams. For the photon beam shielding calculation, S_N transport was applied; for the electron beam shielding calculation, a full physics Monte Carlo calculation can then be performed with EDK. The photon beam energy can operate at 6 MV (6X) or 18 MV (18X). This study presented the 6X operation mode, as the 18X mode would require a photo-neutron study. A spectrum for this analysis, representative of an equivalent 6X spectrum was used, as is shown in Figure 50.
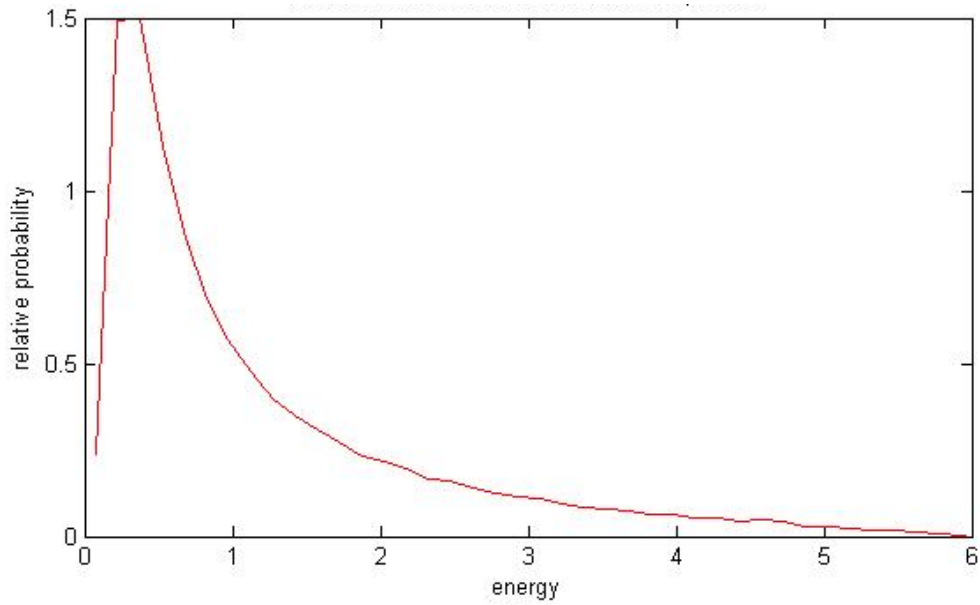
Figure 50. Representative 6X photon spectrum.

The 6MV photon transport calculation was based on a 984 group cross-section, spanning 0 to 24 MeV, adapted from the Sandia National Lab CEPXS code (Lorence, Morel et al. 1989). The resulting 984 group cross-section was then compared to continuous XCOM: Photon Cross Section Data from NIST (NIST 2011). Figure 51 computes both discrete (CEPXS) and continuous XCOM cross-sections for LiF. In the range of 50 keV– 6 MeV, the maximum difference among the discrete cross section and the continuous cross section was designed to be more than 5% in the energy range of interest (50 keV – 6 MeV).
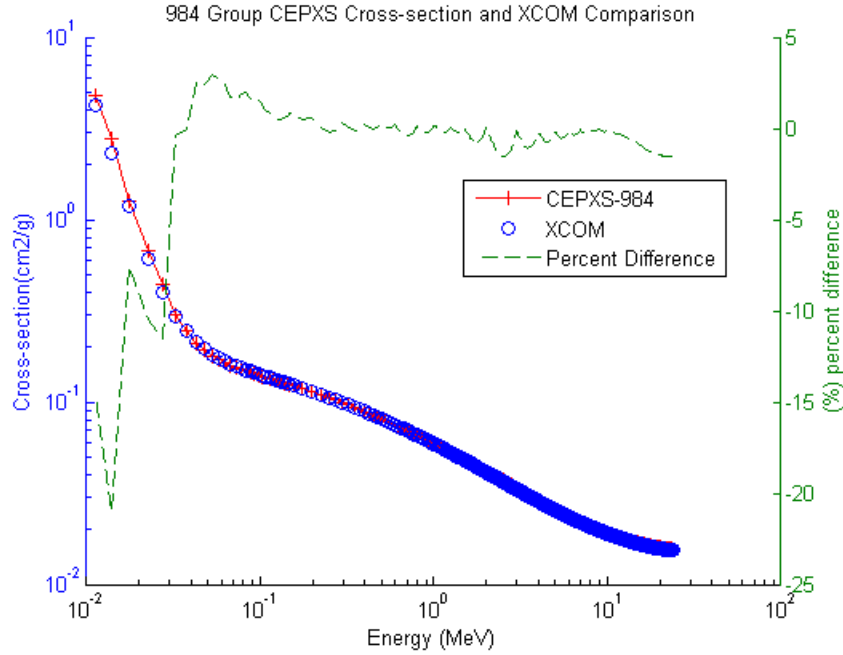
Figure 51. Comparison between 984-group CEPXS generated total cross section and XCOM continuous microscopic cross section for up to 10 MeV photon beam for LiF.

Briefly presenting forward and adjoint detector response, standard texts and references provide for calculation of adjoint detector response with adjoint group importance in a detector volume based on a forward source volume (Bell and Glasstone 1970). A minor adjustment is made so that the partial leakage adjoint function can be used properly in conjunction with a source surface (where normally volumetric sources are considered).

Normally, by considering a forward source in the linear Boltzmann transport equation:

$$
\begin{aligned}
H\psi_g(\mathbf{r},\mu,\varphi) &= S_g(\mathbf{r},\mu,\varphi) && \text{for } \mathbf{r} \in \Gamma \\
H\psi_g(\mathbf{r},\mu,\varphi) &= 0 && \text{for } \mathbf{r} \notin \Gamma
\end{aligned}
\tag{A1.1}
$$

where H is the forward transport operator, ψ_g is the angular flux, S_g is the angular source, and Γ is the detector front surface. Here, the define the forward response and adjoint response are defined as

$$
R_{fwd} = \left\langle \psi_g(\mathbf{r},\mu,\varphi) \cdot \sigma_{\det,g} \right\rangle \quad \text{for } \mathbf{r} \in \Lambda
\tag{A1.2}
$$

$$
R_{adj} = \left\langle \psi^*_g \cdot S_g(\mathbf{r},\mu,\varphi) \right\rangle \quad \text{for } \mathbf{r} \in \Gamma
\tag{A1.3}
$$

85

where the brackets denote integration over the phase space, and ψ^* is the adjoint angular importance function, with Λ as the detector volume.

In the assumption of an isotropic flux, the partial current density is given by $J_+ = \phi/4$. Analogously, the expression in the adjoint form (where it is assumed that the source is isotropic), suggests $J_+^* = \phi^*/4$. It can be shown that this effectively adjusts the adjoint response rate to:

$$R_{adj} = 4\left\langle \left(J_-^*\right)_g \cdot S_g\left(\mathbf{r}\right)\right\rangle \quad \text{for } \mathbf{r} \in \Gamma \tag{A1.4}$$

Adjoint response is then calculated using adjoint group partial leakage given an isotropic surface source.

The initial evaluation constituted a 1D S_N Geometry model using 984 photon groups in an S_{20}, P_3 calculation using PENTRAN (Sjoden and Haghighat 1997), with the application of a 6X source spectrum (supplied as a surface source incident to a 10 cm concrete slab), followed by a 1 cm detector region (LiF or Al_2O_3) using 110 fine meshes. Cross sections of orders P_3, P_7, P_{11} were generated using CEPXS. The adjoint model was constructed by supplying the detector absorption cross section as the source term located in the detector volume.

A1.2 Resulting Adjoint Detector Responses for LiF and Al₂O₃

Figure 52 shows the detector absorption cross sections for Al_2O_3 and LiF to which one

sets to the adjoint source. Figure 53 displays the relative computed adjoint importance (x-axis in

log scale for both figures) on the opposite side of the shield where a source would originate.

Also, Figure 53 indicates that the overall adjoint importance of Al_2O_3 in the range of 0 to 6 MeV

is higher than that of LiF by factor of 3. Preliminary calculations show that adjoint and forward

responses are equivalent, as shown in Equation 4.2, 4.3, and 4.4 (convergence to 1E-4).

The detector flux results are shown using the forward transport model with PENTRAN,

in Figure 54 with a broad peak centered at 80 keV, and sharp peaks at 184.9 keV and 534.8 keV.

In comparison to the continuous energy Monte Carlo (MCNP5) simulation, the same flux peaks

are present. However, in the MCNP5 calculations, the 534.8 keV peak is stronger (not in figure

but indicated by vertical line) compared to the S_N result, due to the multi-group averaging effect

in the calculations. Overall, flux shapes are consistent between Sn and MC calculations.

In conclusion, the adjoint calculations show that Al_2O_3 has a stronger adjoint importance

in the source location than compared to LiF. Also, the 984-group structure and cross section set

are identified to be suitable for future Sn shielding calculations, with both S_N and Monte Carlo

identifying the same broad and sharp peak locations in the energy spectrum for both Al_2O_3 and

LiF. Moreover, dose conversion methods are to be applied to convert photon flux to dose rates.
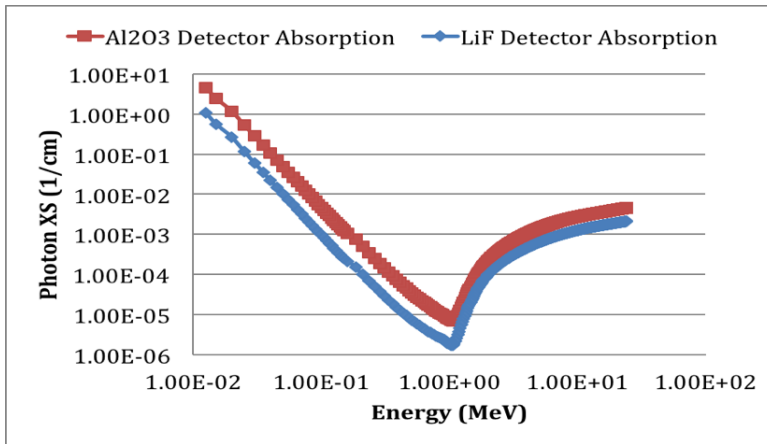
Figure 52. Al$_2$O$_3$ and LiF detector absorption cross sections (1/cm vs E (MeV), log-log plot).
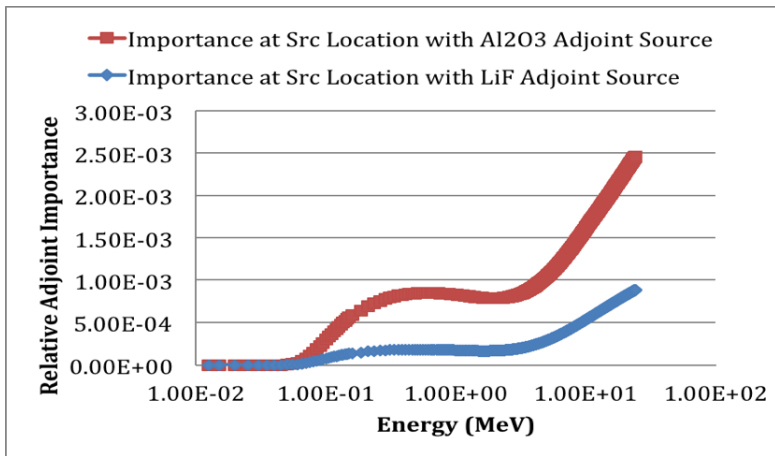
Figure 53. Adjoint importance in source location from S$_N$ Transport with PENTRAN code (log-linear plot).
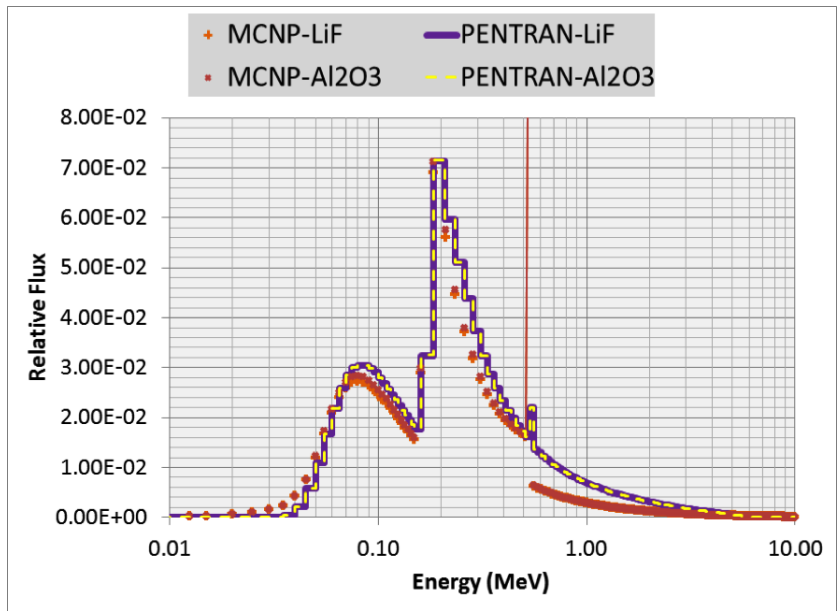
Figure 54. Detector flux results with S_N Transport and MCNP multi-group (average relative error ~1%, log-linear plot).

APPENDIX B

EXAMPLE MCNP (PARTIAL) INPUT DECK USED FOR EDK DOSE

KERNEL GENERATION

```
EDK -  0.5  mesh - by Mi Huang
c
c adjustment of photon importances to 1 in the water phantom cells
c TTB approxmation is on (but may not be an issue when 'mode p e' is used)
c
c this is the new basis run for edk kernel on gt-pace cluster
c
c  -----  begin cell definitions  -----
1     1      -1.0 -1     imp:p=1 imp:e=1 vol=0.125 $ EDK Cell Meshes
c  ----- some cells not shown (too long)
10648 1      -1.0 -10648 imp:p=1 imp:e=1 vol=0.125 $ EDK Cell Meshes
c  ------------------------------------------------------------------
90011 1      -1.0  -90001 : -90002 : -90003 : -90004 : -90005 : -90006 : -90007
       : -90008 : -90009 : -90010 : -90011  imp:p=1 imp:e=1 vol=2662.0 $bottom
90012 1      -1.0  (-90012 90000) imp:p=1 imp:e=1 vol=181.5 $ Outer ring water meshes
90013 1      -1.0  (-90013 90000) imp:p=1 imp:e=1 vol=181.5 $ Outer ring water meshes
90014 1      -1.0  (-90014 90000) imp:p=1 imp:e=1 vol=181.5 $ Outer ring water meshes
90015 1      -1.0  (-90015 90000) imp:p=1 imp:e=1 vol=181.5 $ Outer ring water meshes
90016 1      -1.0  (-90016 90000) imp:p=1 imp:e=1 vol=181.5 $ Outer ring water meshes
90017 1      -1.0  (-90017 90000) imp:p=1 imp:e=1 vol=181.5 $ Outer ring water meshes
90018 1      -1.0  (-90018 90000) imp:p=1 imp:e=1 vol=181.5 $ Outer ring water meshes
90019 1      -1.0  (-90019 90000) imp:p=1 imp:e=1 vol=181.5 $ Outer ring water meshes
90020 1      -1.0  (-90020 90000) imp:p=1 imp:e=1 vol=181.5 $ Outer ring water meshes
90021 1      -1.0  (-90021 90000) imp:p=1 imp:e=1 vol=181.5 $ Outer ring water meshes
90022 1      -1.0  (-90022 90000) imp:p=1 imp:e=1 vol=181.5 $ Outer ring water meshes
90023 1      -1.0  (-90023 90000) imp:p=1 imp:e=1 vol=181.5 $ Outer ring water meshes
90024 1      -1.0  (-90024 90000) imp:p=1 imp:e=1 vol=181.5 $ Outer ring water meshes
90025 1      -1.0  (-90025 90000) imp:p=1 imp:e=1 vol=181.5 $ Outer ring water meshes
90026 1      -1.0  (-90026 90000) imp:p=1 imp:e=1 vol=181.5 $ Outer ring water meshes
90027 1      -1.0  (-90027 90000) imp:p=1 imp:e=1 vol=181.5 $ Outer ring water meshes
90028 1      -1.0  (-90028 90000) imp:p=1 imp:e=1 vol=181.5 $ Outer ring water meshes
90029 1      -1.0  (-90029 90000) imp:p=1 imp:e=1 vol=181.5 $ Outer ring water meshes
90030 1      -1.0  (-90030 90000) imp:p=1 imp:e=1 vol=181.5 $ Outer ring water meshes
90031 1      -1.0  (-90031 90000) imp:p=1 imp:e=1 vol=181.5 $ Outer ring water meshes
90032 1      -1.0  (-90032 90000) imp:p=1 imp:e=1 vol=181.5 $ Outer ring water meshes
90033 1      -1.0  (-90033 90000) imp:p=1 imp:e=1 vol=181.5 $ Outer ring water meshes
90034 1      -1.0  -90034 : -90035 : -90036 : -90037 : -90038 : -90039 : -90040
       : -90041 : -90042 : -90043 : -90044  imp:p=1 imp:e=1 vol=2662.0 $top
99999 0       90001 90002 90003 90004 90005 90006 90007 90008 90009 90010
              90011 90012 90013 90014 90015 90016 90017 90018 90019 90020
              90021 90022 90023 90024 90025 90026 90027 90028 90029 90030
              90031 90032 90033 90034 90035 90036 90037 90038 90039 90040
              90041 90042 90043 90044 imp:p,e 0
c  -----  end of cell definitions  -----

c  -----  begin surface definitions  -----
1     rpp   0.0   0.5    0.0    0.5    0.0    0.5
c  -----   some rpps not shown -----
10648 rpp  10.5  11.0   10.5   11.0   10.5   11.0
c  ------------------------------------------------------------------
90000 rpp   0.0  11.0    0.0   11.0    0.0   11.0
90001 rpp  -5.5  16.5   -5.5   16.5   -5.5   -5.0
90002 rpp  -5.5  16.5   -5.5   16.5   -5.0   -4.5
90003 rpp  -5.5  16.5   -5.5   16.5   -4.5   -4.0
90004 rpp  -5.5  16.5   -5.5   16.5   -4.0   -3.5
90005 rpp  -5.5  16.5   -5.5   16.5   -3.5   -3.0
90006 rpp  -5.5  16.5   -5.5   16.5   -3.0   -2.5
```

```
90007 rpp  -5.5  16.5  -5.5  16.5  -2.5  -2.0
90008 rpp  -5.5  16.5  -5.5  16.5  -2.0  -1.5
90009 rpp  -5.5  16.5  -5.5  16.5  -1.5  -1.0
90010 rpp  -5.5  16.5  -5.5  16.5  -1.0  -0.5
90011 rpp  -5.5  16.5  -5.5  16.5  -0.5   0.0
90012 rpp  -5.5  16.5  -5.5  16.5   0.0   0.5
90013 rpp  -5.5  16.5  -5.5  16.5   0.5   1.0
90014 rpp  -5.5  16.5  -5.5  16.5   1.0   1.5
90015 rpp  -5.5  16.5  -5.5  16.5   1.5   2.0
90016 rpp  -5.5  16.5  -5.5  16.5   2.0   2.5
90017 rpp  -5.5  16.5  -5.5  16.5   2.5   3.0
90018 rpp  -5.5  16.5  -5.5  16.5   3.0   3.5
90019 rpp  -5.5  16.5  -5.5  16.5   3.5   4.0
90020 rpp  -5.5  16.5  -5.5  16.5   4.0   4.5
90021 rpp  -5.5  16.5  -5.5  16.5   4.5   5.0
90022 rpp  -5.5  16.5  -5.5  16.5   5.0   5.5
90023 rpp  -5.5  16.5  -5.5  16.5   5.5   6.0
90024 rpp  -5.5  16.5  -5.5  16.5   6.0   6.5
90025 rpp  -5.5  16.5  -5.5  16.5   6.5   7.0
90026 rpp  -5.5  16.5  -5.5  16.5   7.0   7.5
90027 rpp  -5.5  16.5  -5.5  16.5   7.5   8.0
90028 rpp  -5.5  16.5  -5.5  16.5   8.0   8.5
90029 rpp  -5.5  16.5  -5.5  16.5   8.5   9.0
90030 rpp  -5.5  16.5  -5.5  16.5   9.0   9.5
90031 rpp  -5.5  16.5  -5.5  16.5   9.5  10.0
90032 rpp  -5.5  16.5  -5.5  16.5  10.0  10.5
90033 rpp  -5.5  16.5  -5.5  16.5  10.5  11.0
90034 rpp  -5.5  16.5  -5.5  16.5  11.0  11.5
90035 rpp  -5.5  16.5  -5.5  16.5  11.5  12.0
90036 rpp  -5.5  16.5  -5.5  16.5  12.0  12.5
90037 rpp  -5.5  16.5  -5.5  16.5  12.5  13.0
90038 rpp  -5.5  16.5  -5.5  16.5  13.0  13.5
90039 rpp  -5.5  16.5  -5.5  16.5  13.5  14.0
90040 rpp  -5.5  16.5  -5.5  16.5  14.0  14.5
90041 rpp  -5.5  16.5  -5.5  16.5  14.5  15.0
90042 rpp  -5.5  16.5  -5.5  16.5  15.0  15.5
90043 rpp  -5.5  16.5  -5.5  16.5  15.5  16.0
90044 rpp  -5.5  16.5  -5.5  16.5  16.0  16.5
c  -----  end of surface definitions  -----

c  -----  begin data card  -----
mode  p e
m1 01001 -0.11 08016 -0.89 $ H2O
sdef    x=d1 y=d2 z=d3  erg=d4 AXS=0 0 1 dir=1.0  vec=0 0 1
si1  H    5.0 5.5
sp1  D    0 1
si2  H    5.0 5.5
sp2  D    0 1
si3  H    0.0 0.5 $ z-position
sp3  D    0 1
si4  H    7.5 8.0
sp4  D    0 1
c  -----
f14:p 5071 5072 5093 5094 5555 5556 5577 5578 t
f24:p 90022
c
c  -----  'kerma' tally below  -----
c
f16:p 1 10646I 10648 t
c f26:p,e 1 10646I 10648 t
c
E16    0.0  7.5 8.0 $ target line replaced two
c
c  -----  absorbed dose tally below  -----
c
*f18:p,e 1 10646I 10648 t
*f28:p,e 90022
E18    0.0  7.5 8.0 $
E28    0.0  7.5 8.0 $
*f38:e 1 10646I 10648 t
*f48:e 90022
```

```
E38    0.0  7.5 8.0 $
E48    0.0  7.5 8.0 $
c phys:p 4j 1 TTB may not matter so much when 'mode p e' is employed
ctme 4800
c
c  ---- photon cutoff
c
cut:p 1j 7.5 $
prdmp 2j 1
totnu
print
c  -----  end data card  -----
```

REFERENCES

Ahnesjö, A. and M. M. Aspradakis (1999). "Dose calculations for external photon beams in radiotherapy." Physics in Medicine and Biology **44**(11): R99.

Ahnesjö, A., et al. (1992). "A pencil beam model for photon dose calculation." Medical Physics **19**(2): 263-273.

Ahrens, C. and G. Beylkin (2009). Rotationally invariant quadratures for the sphere. Proceedings of the Royal Society of London A: Mathematical, Physical and Engineering Sciences, The Royal Society.

Al-Basheer, A. K., et al. (2009). "Electron dose kernels to account for secondary particle transport in deterministic simulations." Nuclear Technology **168**(3): 906-918.

Al Basheer, A. (2008). 3D deterministic radiation transport for dose computations in clinical procedures. Gainesville, Fla, University of Florida.

Batho, H. (1964). "Lung corrections in cobalt 60 beam therapy." Journal of the Canadian Association of Radiologists **15**: 79.

Bell, G. I. and S. Glasstone (1970). Nuclear Reactor Theory, Van Nostrand Reinhold.

Bolch, W., et al. (2010). "HYBRID COMPUTATIONAL PHANTOMS FOR MEDICAL DOSE RECONSTRUCTION." Radiation and environmental biophysics **49**(2): 155-168.

Bush, K., et al. (2011). "Dosimetric validation of Acuros® XB with Monte Carlo methods for photon dose calculations." Medical Physics **38**(4): 2208-2221.

Capote, R., et al. (2006). "Phase-space database for external beam radiotherapy." IAEA, Nucl. Data Sec. Report INDC (NDS)-0484, International Atomic Energy Agency, Vienna, Austria.

Carlson, B. and G. Bell (1958). Solution of the transport equation by the Sn method, Los Alamos Scientific Lab., N. Mex.

Chetty, I. J., et al. (2007). "Report of the AAPM Task Group No. 105: Issues associated with clinical implementation of Monte Carlo-based photon and electron external beam treatment planning." Medical Physics **34**(12): 4818-4853.

Collette, A. (2013). Python and HDF5, " O'Reilly Media, Inc.".

Constantin, M., et al. (2011). "Modeling the TrueBeam linac using a CAD to Geant4 geometry implementation: Dose and IAEA-compliant phase space calculations." Medical Physics **38**(7): 4018-4024.

Constantin, M., et al. (2011). "SU-E-T-663: Extended TrueBeam Patient-Independent Phase Space Library for the 6X, 6XFFF, 10X and 10XFFF Radiotherapy Beams." Medical Physics **38**(6): 3642-3642.

Constantin, M., et al. (2013). "SU-E-T-504: Electron Beam Tuning Methodology for TrueBeam Phase-Space Library Generation." Medical Physics **40**(6): 321-321.

Dionne, B. (2007). Automated Variance Reduction Technique for 3-D Monte Carlo Coupled Electron-Photon-Positron Simulation Using Deterministic Importance Functions, University of Florida.

El-Khatib, E. and J. Battista (1984). "Improved lung dose calculation using tissue−maximum ratios in the batho correction." Medical Physics **11**(3): 279-286.

Failla, G., et al. (2011). Acuros XB advanced dose calculation for the Eclipse treatment planning system (White Paper). Palo Alto, California, Varian Medical Systems**:** 32.

Fogliata, A., et al. (2007). "On the dosimetric behaviour of photon dose calculation algorithms in the presence of simple geometric heterogeneities: comparison with Monte Carlo calculations." Physics in Medicine and Biology **52**(5): 1363.

Huang, M., et al. (2012). A New Approach for Shielding Calculation on Clinac iX Linear Accelerator Vault using Discrete Ordinates Radiation Transport Method. American Nuclear Society Winter Meeting and Nuclear Technology Expo, San Diego, American Nuclear Society.

Huang, M., et al. (2009). Optimization of electron dose kernels to account for heterogeneities in voxelized phantoms. Proc. IEEE Proceedings, Orlando, FL.

Huang, M., et al. (2010). "SU-GG-T-408: Validation of a Novel Dose Calculation Approach for Heterogeneous Voxelized Phantoms in a Parallel Computation Environment Using Electron Dose Kernels for Radiotherapy." Medical Physics **37**(6): 3280-3280.

Hyödynmaa, S. (1994). Electron beam dose computation using generalized Gaussian pencil beam algorithm with 3-D inhomogeneity correction and arbitrary fields shapes. Proceedings of the tenth international conference on the use of computers in radiation therapy, Manchester.

Khan, F. M. and J. P. Gibbons (2014). Khan's the Physics of Radiation Therapy, Lippincott Williams & Wilkins.

Knöös, T., et al. (2006). "Comparison of dose calculation algorithms for treatment planning in external photon beam therapy for clinical situations." Physics in Medicine and Biology **51**(22): 5785.

Krieger, T. and O. A. Sauer (2005). "Monte Carlo-versus pencil-beam-/collapsed-cone-dose calculation in a heterogeneous multi-layer phantom." Physics in Medicine and Biology **50**(5): 859.

Kry, S. F., et al. (2006). "A Monte Carlo model for calculating out-of-field dose from a Varian 6MV beam." Medical Physics **33**(11): 4405-4413.

Kutcher, G. J., et al. (1994). "Comprehensive QA for radiation oncology: report of AAPM radiation therapy committee task group 40." Medical Physics **21**: 581-581.

Lathrop, K. D. (1968). "Ray effects in discrete ordinates equations." Nuclear science and engineering **32**(3): 357-369.

Lax, I. (1987). "Accuracy in clinical electron beam dose planning using pencilbeam algorithms." Radiotherapy and Oncology **10**(4): 307-319.

Lee, C., et al. (2008). "Hybrid computational phantoms of the 15-year male and female adolescent: applications to CT organ dosimetry for patients of variable morphometry." Med Phys **35**(6): 2366-2382.

Longoni, G. (2004). Advanced Quadrature Sets, Acceleration and Preconditioning Techniques for the Discrete Ordinates Method in Parallel Computing Environments, University of Florida.

Lorence, L., et al. (1989). Physics Guide to CEPXS: A Multigroup Coupled Electron-Photon Generating Code, Sandia National Laboratory.

Manalo, K., et al. (2013). Advanced quadratures and periodic boundary conditions in parallel 3D S{sub n} transport. M&C 2013.

Mathworks (2015). "MAT-file Versions." 2015, from http://www.mathworks.com/help/matlab/import_export/mat-file-versions.html.

McGinley, P. (2011). Radiation Shielding Evaluation, Varian High Energy Accelerator Boggs Building. Atlanta, GA, Georgia Institute of Technology.

Miften, M., et al. (2001). "Comparison of RTP dose distributions in heterogeneous phantoms with the BEAM Monte Carlo simulation system." Journal of Applied Clinical Medical Physics **2**(1): 21-31.

Mobit, P., et al. (2006). "Comparison of the energy-response factor of LiF and Al2O3 in radiotherapy beams." Radiation protection dosimetry **119**(1-4): 497-499.

NCRP (2005). NCRP Report No. 151, Structrual Shielding Design and Evaluation for Megavoltage X- and Gamma-Ray Radiotherapy Facilities, National Council on Radiation Protection and Measurements.

NIST (2011). XCOM: Photon Cross Sections Database, updated 2011, National Institute of Standards and Technology.

Papanikolaou, N., et al. (2004). "Tissue inhomogeneity corrections for megavoltage photon beams." AAPM Task Group **65**: 1-142.

Scarboro, S. and S. Kry (2013). "Characterisation of energy response of Al2O3: C optically stimulated luminescent dosemeters (OSLDs) using cavity theory." Radiation protection dosimetry **153**(1): 23-31.

Scopatz, A., et al. (2012). PyNE: Python for Nuclear Engineering. American Nuclear Society Winter Meeting 2012, San Diego, CA.

Shalek, R. J. (1977). "Determination of Absorbed Dose in a Patient Irradiated byBeams of X or Gamma Rays in Radiotherapy Procedures." Medical Physics **4**(5): 461-461.

Sievinen, J., et al. (2005). "AAA photon dose calculation model in Eclipse." Palo Alto (CA): Varian Medical Systems **118**: 2894.

Sjoden, G. and A. Haghighat (1997). PENTRAN - A 3-D Cartesian Parallel Sn Code with Angular, Energy, and Spatial Decomposition. Proceedings of ANS M&C, Saratoga Springs, NY.

Sjoden, G. E. (1997). PENTRAN: A parallel 3-D S(N) transport code with complete phase space decomposition, adaptive differencing, and iterative solution methods. Ann Arbor, The Pennsylvania State University. **9732375:** 301-301 p.

Sjoden, G. E. (2007). "An Efficient Exponential Directional Iterative Differencing Scheme for Three-Dimensional S n Computations in XYZ Geometry." Nuclear science and engineering **155**(2): 179-189.

Stovall, M., et al. (1995). "Fetal dose from radiotherapy with photon beams: report of AAPM Radiation Therapy Committee Task Group No. 36." Medical Physics **22**(1): 63-82.

The HDF Group (1997-2015). "Hierarchical Data Format, version 5." from http://www.hdfgroup.org/HDF5.

Thomas, S. J. (1991). "A modified power-law formula for inhomogeneity corrections in beams of high-energy x rays." Medical Physics **18**(4): 719-723.

Ulmer, W. and D. Harder (1995). "A triple Gaussian pencil beam model for photon beam treatment planning." Zeitschrift für medizinische Physik **5**(1): 25-30.

Vanhavere, F., et al. (2004). "Peripheral neutron and gamma doses in radiotherapy with an 18 MV linear accelerator." Radiation protection dosimetry **110**(1-4): 607-612.

Varian (2011). Eclipse Algorithms Reference Guide, Varian Medical Systems.

Wong, J. W. and J. A. Purdy (1990). "On methods of inhomogeneity corrections for photon transport." Medical Physics **17**(5): 807-814.

Yi, C. (2007). Hybrid discrete ordinates and characteristics method for solving the linear Boltzmann equation. Nuclear Engineering, University of Florida. **PhD Thesis**.

VITA

Mi Huang

Mi Huang attended the University of Florida and Georgia Institute of Technology for graduate studies in medical physics. She obtained both Master of Electrical and Computer Engineering and Master of Medical Physics degrees from University of Florida. During her graduate studies at Georgia Tech, she completed an NNSA neutron detection project and the 3D EDK-S_N application for radiation therapy dose calculation for Ph.D. medical physics projects. She was also actively involved in the GT RSEL research and teaching assistant duties for students, and multiple clinical medical physics projects with University of Florida and GT/Emory program.